Redirection of SARS-CoV-2 to Phagocytes by Intranasal sACE2-Fc as a Universal Decoy Confers Complete Prophylactic Protection

Jingyi Wang[a]†, Jiangchuan Li[a]†, Alex W. Chin[b,c]†, Bin Luo[a,d], Junkang Wei[a], Jiale Qiu[a], Jianwei Ren[a,d], Yin Xia[a], Thomas Braun[a,e], Leo L.M. Poon[b,c,f]*, Bo Feng[a,d,g]*

[a] School of Biomedical Sciences, Faculty of Medicine; GIBH CAS-CUHK Joint Research Laboratory on Stem Cell and Regenerative Medicine, The Chinese University of Hong Kong; Hong Kong SAR, China.

[b] School of Public Health, LKS Faculty of Medicine, The University of Hong Kong; Hong Kong SAR, China.

[c] Centre for Immunology & Infection, Hong Kong Science and Technology Park; Hong Kong SAR, China.

[d] Centre for Regenerative Medicine and Health, Hong Kong Institute of Science & Innovation, Chinese Academy of Sciences; Hong Kong SAR, China.

[e] Department of Cardiac Development and Remodeling, Max-Planck-Institute for Heart and Lung Research, 61231, Bad Nauheim, Germany.

[f] HKU-Pasteur Research Pole, LKS Faculty of Medicine, The University of Hong Kong; Hong Kong SAR, China.

[g] Guangzhou Institutes of Biomedicine and Health, Chinese Academy of Sciences; Guangzhou 510530, China.

* Corresponding authors. Email: llmpoon@hku.hk (L.L.P.); fengbo@cuhk.edu.hk (B.F.).

† These authors contribute equally.

ABSTRACT

The rapid evolution of SARS-CoV-2 and other respiratory RNA viruses limits the success of current vaccines and antibody-based therapies. Engineered decoy receptors based on soluble angiotensin-converting enzyme 2 (sACE2) offer promising alternatives. Clinical-grade recombinant sACE2 inhibits SARS-CoV-2 replication *in vitro* but shows limited clinical success. This study reports an optimized sACE2 mutant fused to human IgG1 Fc (B5-D3), which redirects virus–decoy complexes to lysosomal degradation in macrophages. Intranasal prophylactic delivery of B5-D3 confers complete protection in SARS-CoV-2-infected K18-hACE2 mice. Abrogation of Fc effector functions compromises antiviral protection, indicating that Fc-mediated uptake of virus–decoy complexes is critical. Transcriptomic analysis suggests that B5-D3 induces early immune activation in lungs of infected mice. Bio-distribution and flow cytometry reveal selective targeting of airway phagocytes. *In vitro* assays confirm lysosomal degradation of virus–decoy complexes by macrophages without productive infection. These findings reveal a distinct antiviral mechanism via phagocytic clearance, supporting refined regimens for decoy treatments against SARS-CoV-2 and potentially other respiratory viruses.

KEYWORDS

sACE2-Fc, SARS-CoV-2, intranasal prophylaxis, Fc-mediated effector function, phagocytosis, decoy receptor

INTRODUCTION

The incessant evolution of severe acute respiratory syndrome coronavirus 2 (SARS-CoV-2) and frequent breakthrough infections during the coronavirus disease 2019 (COVID-19) pandemic

underscore the critical need for effective antiviral strategies that are less susceptible to immune escape than conventional vaccines and monoclonal antibody (mAb) therapies [1].

Soluble angiotensin-converting enzyme 2 (sACE2) therapies, which employ recombinant forms of the human angiotensin-converting enzyme 2 (ACE2) receptor—the primary binding site for the SARS-CoV-2 spike protein [1-5]—as viral decoys, have emerged as a promising alternative [6]. However, an early clinical version (amino acid [aa] 1-740, APN01) showed limited therapeutic benefit [7] and raised safety concerns about interference with endogenous renin-angiotensin system (RAS) [8]. Subsequent protein engineering greatly improved the pharmacological properties of sACE2, including fusion with a human IgG1 Fc domain (sACE2-Fc) to enhance serum half-life [9], and mutagenesis to enhance spike-binding affinity [10-12] and abolish enzymatic activity [10, 12, 13]. Potent sACE2-Fc mutants have shown broad-spectrum neutralization against SARS-CoV-2 variants in animal models [14-16]. However, their efficacy in protecting hosts from viral infections was often incomplete. Despite the evidence suggesting a role for Fc-mediated effector functions in sACE2-Fc efficacies [14], underlying immune mechanisms remained poorly understood. Further investigation that systematically assesses the potential to optimize decoy design, strategies of administration, and mechanisms of actions is pivotal to the development of ACE2 decoy-based antivirals and harnessing their full potential.

In this study, we engineered a potent yet minimally mutated sACE2-Fc decoy candidate (B5-D3) with just two mutations to enhance spike-binding (T92Q) while eliminating enzymatic activity (H374N). Broad-spectrum neutralization capacity against multiple SARS-CoV-2 variants was confirmed by *in vitro* neutralization assays. Markedly, stepwise examinations of various administration routes and time points identified intranasal (IN) prophylaxis as the most effective regimen for B5-D3, which conferred complete protection against SARS-CoV-2 infection in K18-hACE2 mice across age groups. Whereas B5-D3 intravenously administered either prior or post

infection, showed activity that moderately improved disease outcome. To understand how sACE2-Fc decoys influence viral fate and achieve superior antiviral protection via IN prophylaxis, we carried out systematic, mechanistic investigations through transcriptomics, bio-distribution, and phagocytosis analysis. Our results revealed that IN-delivered B5-D3 engages airway phagocytes to promote early viral clearance and host immune activation, which uncovers a distinct antiviral mechanism and offers a universal and commonly applicable "decoy strategy" to combat unknown air-borne respiratory virus in the future.

RESULTS

Engineered sACE2-Fc decoys with two single mutations achieve robust neutralization against SARS-CoV-2 variants

To generate representative ACE2 decoys with optimal performance, we adopted the established sACE2-Fc fusion design [9] (Fig. 1a; Supplementary Fig. 1) and selectively verified mutation(s) proposed in prior studies, either to enhance the binding of human ACE2 to SARS-CoV-2 spikes [17] (B2–B6) or to abolish enzymatic activity [10-12, 18] (A2, A3, D1–D5) (Supplementary Fig. 2a,b). The sACE2-Fc candidates generated with either type of mutation(s) were all verified for pseudovirus-based neutralization assays [19] and ACE2 enzymatic activity. Indeed, mutants B2–B6 showed consistently enhanced neutralization capacity against both Wuhan-Hu-1 and D614G pseudoviruses [20] (Fig. 1b; Supplementary Fig. 2c,d). Notably, B5 with the single T92Q mutation, which increases spike affinity by removing a critical glycosylation site at N90 [21], exhibited remarkable neutralization enhancement among other multi-mutants. Meanwhile, mutations selected for catalytic inactivation, including the previously reported mutation pairs A2 [11, 18], A3 [10], single mutations derived from these pairs (D1, D3, D4, but not D2), and a recently reported single mutation D5 [12], effectively abolished enzymatic activity while showing minimal effect on spike binding (Fig. 1b; Supplementary Fig. 2e). We next combined

98 the B5 (T92Q) mutation with each of the inactivating mutations. Notably, among the resulting
99 compound mutants, B5-D1, B5-D3, B5-D4, and B5-D5 with two mutations remained to be
100 enzymatically inactive while retaining comparable or stronger neutralization capacity than B5-
101 A2 and B5-A3 with three mutations (Fig. 1b; Supplementary Fig. 2f–h). B5-D3 (T92Q/H374N)
102 emerged as one of the best candidates (Fig. 1a, red stars; Fig. 1b, red arrow), exhibiting minimal
103 deviation from wild type (WT) ACE2 in structural modeling (root mean square deviation [RMSD]
104 = 0.212 Å; Supplementary Fig. 2i) [22].

105 To assess the breadth of neutralization, we tested three double mutants (B5-D3, B5-D4, and B5-
106 D5) against pseudoviruses bearing spikes from various variants of concern (VOCs) and variants
107 of interest (VOIs) [1, 23-27]. All three designs showed dose-dependent neutralization with higher
108 potency than WT sACE2-Fc (Fig. 1c,d; Supplementary Fig. 3). We further examined B5-D3, as
109 a representative decoy candidate, against authentic SARS-CoV-2 using plaque reduction
110 neutralization tests (PRNTs) in Vero E6 cells, which indeed, confirmed its robust activity against
111 Wuhan-Hu-1, Delta, and Omicron variants BA.5, BQ.1.22, and XBB.1.5 strains [1, 24, 28, 29]
112 (Fig. 1e-g). In contrast, Casirivimab, serving as positive control [30], showed efficacy only
113 against early variants (Wuhan-Hu-1 and Delta; Fig. 1f), but failed to neutralize Omicron
114 sublineages (Fig. 1g). These results demonstrate that a rationally engineered sACE2-Fc decoy
115 with only two mutations could achieve potent and safe neutralization across SARS-CoV-2
116 variants, reducing the potential risks associated with extensive mutagenesis.

117

118 **Prolonged *in vivo* overexpression of sACE2-Fc double mutants demonstrates minimal RAS**
119 **disturbance and no tissue damage in mice**

120 Next, we evaluated the safety of the sACE2-Fc double mutants *in vivo* (Supplementary Fig. 4a).
121 Adult K18-hACE2 transgenic mice with immune tolerance to human ACE2 [31] were
122 intravenously injected with adenovirus-associated virus (AAV) vectors encoding either WT

sACE2-Fc or double mutants at a dose of 1×10^{11} genome copies (GC) per mouse. Notably, serum levels of the double mutants (B5-D3, B5-D4, and B5-D5) were significantly higher than those of WT sACE2-Fc (Supplementary Fig. 4b; Supplementary Table 1). This trend was further supported by quantification of AAV genomes in the liver, indicating greater *in vivo* stability or tolerance of the double mutants (Supplementary Fig. 4c).

Importantly, despite prolonged high-level expression, ELISA measurements of serum renin, Angiotensin II (Ang II), and Ang (1–7) [8] demonstrated minimal disturbance to the RAS in mice treated with the double mutants (Supplementary Fig. 4d–f). In contrast, WT sACE2-Fc treatment led to significantly elevated serum levels of renin and Ang II, indicating a disruption of the RAS (Supplementary Fig. 4d,e). Histological examination of multiple organs at the end point showed no evidence of tissue damage in any of these groups (Supplementary Fig. 4g). These observations collectively underscore the improved safety of catalytically inactive sACE2-Fc mutants, supporting their suitability for prolonged or repeated use.

Prophylactic administration of the sACE2-Fc B5-D3 mutant via the intranasal route exhibits superior protection against SARS-CoV-2

Next, we evaluated the *in vivo* efficacy of the sACE2-Fc double mutant B5-D3 against SARS-CoV-2 infection using aged K18-hACE2 mice (10 – 12 months old) (Fig. 2a). 6 hours (h) before inoculating with 1×10^4 plaque-forming unit (PFU) of SARS-CoV-2 (Wuhan-Hu-1 strain), mice received a prophylactic dose of recombinant B5-D3 protein either intranasally (IN, 2.5 mg/kg) or intravenously (IV, 15 mg/kg). To simulate a therapeutic intervention, an additional group received IV B5-D3 (15 mg/kg) 24 h post-virus inoculation. The vehicle control group received an intranasal PBS administration 6 h before viral challenge. Over a 14-day observation period, all mice in the PBS group exhibited significant weight loss and succumbed to infection by 7 days post-infection (dpi) (Fig. 2b,c, black lines). Both IV-treated groups exhibited initial weight loss

148 similar to the PBS group; however, two out of four mice in each group began to regain weight
149 from 10 dpi and survived until the observation endpoint, suggesting improvement in disease
150 severity and survival (green and blue lines). Notably, all mice in the IN-prophylaxis group,
151 despite receiving a 6-fold lower dose of B5-D3 protein than those in the IV groups, maintained
152 stable body weight and achieved complete survival over the 14-day period (red lines).

153 To monitor viral burden, one mouse from each group was sacrificed at 4 dpi (Fig. 2a).
154 Corroborating the body weight and survival data, no infectious viral particles were detected in
155 lung homogenate from the IN-prophylaxis mouse. In contrast, mice treated with IV prophylaxis
156 or therapy showed reduced but still detectable viral titers compared to the PBS group (Fig. 2d).
157 Immunohistochemistry (IHC) staining further confirmed the absence of viral nucleocapsid (N)
158 protein in the IN-treated mouse, whereas IV-treated mice showed residual infection and immune
159 cell infiltration. H&E staining revealed varying degrees of alveolar thickening in all SARS-CoV-
160 2-inoculated mice (Fig. 2e).

161 To further explore the effective timing of IN administration that offers superior antiviral
162 protection, we treated a younger cohort of K18-hACE2 mice (2 – 3 months old) with B5-D3 (IN,
163 2.5 mg/kg) at –24 h, –6 h, or +24 h relative to viral challenge (Fig. 2f). Consistently, all mice in
164 the PBS group of the young cohort exhibited substantial weight reduction from 4 dpi and reached
165 approximately 20% loss by 7 dpi (Fig. 2g, black lines). Whereas differently from the aged cohort,
166 two of the five infected young mice eventually recovered, resulting in 40% survival (Fig. 2g,h,
167 black lines) indicating age-related fitness [32]. Interestingly, both the –24 h and –6 h IN-
168 prophylaxis groups maintained stable body weights (Fig. 2g, pink and red lines), ending up with
169 survival rates of 80% and 100%, respectively (Fig. 2h). In contrast, the +24 h IN-therapy group
170 showed substantial weight loss and no survival improvement compared to the PBS group,
171 indicating that high-efficiency antiviral protection of IN B5-D3 is limited to prophylactic
172 administration but not post-infection treatments (Fig. 2g,h, orange lines). Consistently, virus-

173 neutralizing antibodies were detected in surviving mice from the PBS and +24 h groups at 14
174 dpi, indicating once active infection and subsequent immune response. Whereas antibody levels
175 remained minimal in the two IN-prophylaxis groups, suggesting effective prevention of viral
176 replication (Fig. 2i).

177

178 **Efficient protection against SARS-CoV-2 by intranasal B5-D3 prophylaxis depends on Fc-**
179 **mediated effector functions**

180 Adding on to the 2-week observation of the significant protection conferred by IN prophylaxis
181 with B5-D3, we examined the early responses following SARS-CoV-2 challenge in K18-hACE2
182 mice. A new cohort of 2- to 3-month-old mice received B5-D3 IN treatment 6 h before infection
183 (–6 h), and lung tissues were harvested at 1, 2, and 4 dpi for analysis (Fig. 3a). An additional
184 group was treated with a modified version of B5-D3, which contains L234A/L235A mutations
185 in the human IgG1 Fc region (B5-D3-LALA) to abolish its binding to Fc gamma receptor (FcγR)
186 and abrogate Fc effector functions [33] (Supplementary Fig. 5). Quantitative PCR of viral spike
187 (*S*) and nucleocapsid (*N*) RNA in lung tissues revealed only marginal viral loads in the B5-D3-
188 treated mice at as early as 1 dpi, indicating efficient suppression of early viral replication
189 compared to the PBS group (Fig. 3b). Analysis of infectious viral particles in lung homogenates
190 further corroborated these observations, demonstrating minimal or undetectable viral titers in the
191 B5-D3 group at all time points (Fig. 3c). In contrast, PBS-treated mice exhibited consistently
192 high viral loads. Interestingly, the analysis of B5-D3-LALA group detected varied levels of *S*
193 and *N* RNAs and significant viral burdens in two out of three mice, indicating partial protection
194 and supporting that Fc effector functions are indispensable for full efficacy of IN B5-D3 (Fig.
195 3b,c, right panels). Consistently, IHC staining for N protein in lung sections confirmed the
196 absence of viral infection in the B5-D3 groups at all time points. Whereas signs of viral
197 replication were evident in the lungs of mice treated with PBS since as early as 1 dpi and in the

198 B5-D3-LALA-treated cohort as examined at 4 dpi (Fig. 3d; Supplementary Fig. 6, left panels).
199 Despite variations in viral burden, H&E staining indicated alveolar septal thickening in all
200 groups (Fig. 3e; Supplementary Fig. 6, right panels; Supplementary Fig. 7). Notably, moderate
201 alveolar thickening persisted in the B5-D3-treated mice till the end point at 4 dpi, whereas the
202 PBS groups developed much severer alveolar thickening at 4 dpi. Consistent with the partial
203 protection observed with B5-D3-LALA, histological analysis of lung samples in this group
204 revealed severer yet heterogenous alveolar thickening (Supplementary Fig. 7). These findings
205 collectively demonstrated that IN prophylaxis with B5-D3 blocks SARS-CoV-2 infection not
206 only by neutralization but also by immune mechanisms such as Fc-mediated effector functions.

207

208 **RNA-Seq analysis of lung transcriptomes reveals early antigen presentation and prompt**
209 **viral clearance following SARS-CoV-2 neutralization by B5-D3**

210 To delineate the immune mechanisms underlying IN B5-D3-mediated prophylactic protection
211 against SARS-CoV-2, we examined the transcriptomes of lung samples collected at 1, 2, and 4
212 dpi from the above experiment (Fig. 4a–d; Supplementary Fig. 8a). Unsupervised clustering
213 based on Pearson correlation distinguished samples with severe infection (mainly PBS-treated)
214 from those with subtle or no infection (mocks and most decoy-treated mice) (Supplementary Fig.
215 8a). Corroborating the levels of viral infections observed, differential gene expression (DGE)
216 analysis revealed extensive inflammatory responses in the PBS groups, significantly greater than
217 in mock treatments. At 1, 2, and 4 dpi, 26, 1232, and 1756 genes were upregulated, respectively,
218 and were significantly enriched in Gene Ontology Biological Process (GOBP) terms related to
219 antiviral responses such as type I interferon (IFN) responses and innate immune responses (Fig.
220 4a,b; Supplementary Fig. 8b–d) [34]. In stark contrast, DGE analysis between B5-D3
221 prophylaxis and mocks at 1, 2, and 4 dpi showed subtle changes, with only 1, 7, and 32 genes
222 upregulated, respectively, and only moderate enrichment in chemotaxis-related pathways at 4

223 dpi (Fig. 4c; Supplementary Fig. 8e). The B5-D3-LALA group, however, had 264 genes
224 upregulated at 4 dpi compared to the mocks, suggesting incomplete protection and ongoing viral
225 activity (Fig. 4d; Supplementary Fig. 8f).

226 To capture the immune activations specifically linked to B5-D3-triggered antiviral efficacy other
227 than infection-induced inflammation, we directly compared the B5-D3 and PBS groups (Fig. 4e-
228 j; Supplementary Fig. 9 and 10). Interestingly, at 1 dpi, the B5-D3 group exhibited enhanced
229 expression of several immune-related genes, including *Lef1* [35], *Fscn1* [36], *Kcne4* [37], *Tcrb*,
230 and *Ccl22* [38, 39], which are associated with early dendritic cell function and T cell activation
231 (Fig. 4e). Gene Set Enrichment Analysis (GSEA) of GOBPs and Kyoto Encyclopedia of Genes
232 and Genomes (KEGG) pathways further supported these findings (Fig. 4f,g). Chemotaxis and
233 pathways related to antigen presentation such as Rap1 signaling pathway [40] and Th1 and Th2
234 cell differentiation were significantly activated in the B5-D3 group at 1 dpi compared to PBS
235 group (Fig. 4h-j; Supplementary Fig. 9a–c). Moreover, the B5-D3 groups showed enhancement
236 in cilium movement and metabolism of xenobiotics at both 2 and 4 dpi, suggesting active
237 clearance of viral particles due to effective early responses (Supplementary Fig. 10c–f).

238 Furthermore, we collectively examined the GOBPs that were significantly activated in B5-D3
239 groups at either 1, 2, or 4 dpi among all treatment groups and time points. Markedly, B5-D3
240 group showed higher normalized enrichment scores (NES) in chemotaxis-related GOBP
241 pathways than PBS group at 1 dpi (Fig. 4k, purple boxes), while direct comparison between B5-
242 D3 and PBS groups further revealed the broad involvement of multiple types of effector immune
243 cells (Fig. 4l, purple box). These results collectively indicate that early immune activation is a
244 hallmark of B5-D3-mediated protection.

245 Finally, the lung transcriptomes from mice receiving B5-D3 without viral inoculation showed
246 high similarity to the PBS vehicle controls (Supplementary Fig. 11a). The 10 upregulated genes
247 identified showed poor correlation with the virus-inoculated B5-D3 group (Supplementary Fig.

11b,c), supporting that early immune responses observed in B5-D3 IN prophylaxis groups were primarily triggered by virus neutralization rather than by B5-D3 alone.

Intranasally delivered B5-D3 is enriched in the respiratory tract and targets mainly the airway macrophages

The superior prophylactic antiviral effects of IN over IV administration of B5-D3 as observed in the K18-hACE2 infection experiments (Fig. 2a–e) suggested the importance of mobilizing the local immunity within the respiratory tract. Next, we labeled B5-D3 protein with Alexa Fluor 750 (AF750) and examined its bio-distribution and kinetics after IN administration (Fig. 5a). *In vivo* imaging showed that fluorescence-labeled B5-D3 (B5-D3-AF750) was present in the nasal cavities for at least 24 h after a single IN dose in K18-hACE2 mice (Fig. 5b). *Ex vivo* images further revealed that B5-D3-AF750 distributed in the respiratory tract from nasal cavity to lung within 20 min and remained enriched in lungs by 24 h after administration (Fig. 5c). In contrast, non-respiratory organs showed minimal signals, which were merely detectable in urinary system and liver (Fig. 5d).

To identify the immune cells in the respiratory tract that are actively engaged with IN B5-D3, we performed flow cytometry analysis on bronchoalveolar lavage fluid (BALF) at 6 h after IN administration of B5-D3-AF750 (Fig. 5e). Like normal conditions, over 95% of live BALF cells were $CD45^+$ immune cells, predominantly composed of $CD11c^+$Siglec-F^+ resident alveolar macrophages (AMs) (> 50%) in both treatment and vehicle groups (Fig. 5f; Supplementary Fig. 12). Notably, the IN administered B5-D3-AF750 was actively retained in the $CD45^+$ cells, with positive rates exceeding 65% in all treated mice (Fig. 5g). Among the $CD45^+$B5-$D3^+$ cells, more than 95% were macrophages, composed primarily of $CD11c^+$Siglec-F^+ AMs (87.2 – 91.7%) and Siglec-$F^-$$CD11b^-$$F4/80^+$ monocyte-derived macrophages (mono-Macs; 6.6 – 9.9%) (Fig. 5h, red arrows). Consistently, these macrophage populations also exhibited the highest B5-D3 positive

273 rates (Fig. 5i,j; Supplementary Fig. 13) and greatest median fluorescent intensities (MFI) (Fig.
274 5k, red arrows) among all immune cell types in the BALF, indicating the strongest B5-D3-AF750
275 uptake. Other phagocytic cell types such as the type 2 conventional dendritic cells (cDC2) and
276 monocytes also exhibited considerable AF750 intensities (Fig. 5k, blue arrows; Supplementary
277 Fig. 13b,c), suggesting potential relationships between B5-D3 uptake and phagocytic activities.
278 Confocal microscopy of BALF cells after immunostaining further confirmed that the B5-D3-
279 AF750 were present in the cytoplasm after being retained in AMs (Fig. 5l). These results
280 demonstrate that IN B5-D3 preferentially accumulates in the respiratory tract and is
281 predominantly taken up by airway macrophages, supporting their important role in mediating
282 early immune responses.

283

284 **sACE2-Fc facilitates phagocytosis of SARS-CoV-2 pseudovirus via mechanisms distinct**
285 **from ACE2-dependent viral infection**

286 To examine the implication of macrophage involvement in the early immune activation observed
287 in IN B5-D3 treatment groups, we performed cellular analysis using THP-1 cells as an *in vitro*
288 model for phagocytes [41] and examined the sACE2-Fc-dependent phagocytosis of spike-
289 pseudotyped lentiviruses. Indeed, immunostaining of HIV capsid protein p24 confirmed the
290 attachment and entry of pseudoviruses in the THP-1 cells in a B5-D3-dependent manner, with
291 an evidenced signal peak at 6 h post-co-incubation (Supplementary Fig. 14). Interestingly,
292 analysis on the THP-1-derived M0 and M1 macrophages detected even greater p24 signals,
293 indicating stronger phagocytosis activities compared to undifferentiated THP-1 cells (Fig. 6a,b;
294 Supplementary Fig. 15a,b,d,e). This process resembled antibody-dependent cellular
295 phagocytosis (ADCP), which is significant in THP-1-derived M0 and M1 macrophages [42].
296 Consistently, further examination revealed colocalization of internalized pseudovirus with
297 lysosomal associated membrane protein 1 (LAMP1), indicating trafficking to lysosomes

potentially for degradation [43] (Fig. 6c; Supplementary Fig. 15c,f).

We further examined the pseudovirus uptake in Calu-3 cells overexpressing human ACE2 (hACE2-Calu-3; Supplementary Fig. 16) as a model of lung epithelial cells. In contrast to that in macrophages, co-incubation with B5-D3 significantly reduced the pseudovirus entry in hACE2-Calu-3 cells (Fig. 6d–f). Interestingly, while the pseudovirus transduction in hACE2-Calu-3 cells, in the absence of B5-D3, produced robust luciferase signal indicating viral genome release after cell entry, the evident pseudovirus uptake facilitated by B5-D3 in the THP-1 and derivative macrophages yielded no detectable luciferase activity, which further supported viral degradation within phagolysosomes (Fig. 6g). Corroborating these observations, western blot analysis showed absence of cleaved S2′ fragments in the macrophages that had internalized pseudovirus-B5-D3 complexes, supporting that the pseudoviruses did not undergo membrane fusion or cytosolic release as it did in the epithelial cell model [44] (Fig. 6h).

To evaluate the contribution of Fc-mediated effector functions to virus uptake in macrophages, we further compared the efficiencies of B5-D3, B5-D3-LALA, and hIgG1 isotype in mediating pseudovirus uptake by THP-1-derived macrophages (Supplementary Fig. 17). As indicated by p24 staining, functional impairment (LALA mutations) of Fc in B5-D3 significantly reduced the efficiency of virus uptake, emphasizing the importance of intact Fc in B5-D3 function as decoy. Whereas presence of hIgG1 isotype control showed no impact on pseudovirus uptake, supporting that the phagocytosis was largely specific to the pseudovirus-decoy complexes.

To further evaluate the responses triggered by the pseudovirus-B5-D3 complex in macrophages, we performed RNA-seq analysis. The transcriptomic profiling revealed little difference and identified no DEG between the macrophages incubated with both pseudovirus and B5-D3 and those treated with pseudovirus only (Supplementary Fig. 18a). Whereas interestingly, GSEA detected broad activation of pathways related to antiviral response and macrophage activation in the macrophages internalizing pseudovirus and B5-D3 (Supplementary Fig. 18b–i),

323 corresponding to ADCP effect. These findings indicate moderate immune activation triggered by
324 phagocytosis of pseudovirus-decoy complexes, corroborating with the mild immune activation
325 that accelerated antiviral responses in our mice infection experiments.

326 Collectively, these findings suggest that IN B5-D3 not only blocks viral entry into epithelial cells
327 but also actively redirects SARS-CoV-2 to phagocytic clearance by engaging airway phagocytes
328 via Fc-dependent mechanisms. Moreover, such ADCP-like process contributes to early immune
329 activation and restricts the infection at the respiratory mucosal surface.

330

331 **DISCUSSION**

332 In this study, we comprehensively evaluated the protective efficacy and mechanistic basis of an
333 optimized representative sACE2-Fc decoy (B5-D3) against SARS-CoV-2 infection. By
334 introducing only two mutations (T92Q and H374N), we generated a minimally engineered
335 sACE2-Fc mutant (B5-D3) that achieved broad-spectrum neutralization with minimal risk of
336 disrupting the RAS. Among various administration routes and dosing schedules examined, we
337 demonstrated that IN prophylaxis of B5-D3 achieved the most robust protection, completely
338 preventing disease in both young and aged K18-hACE2 mice. Transcriptomic analysis of the
339 infected lung samples at early time points revealed distinct IN B5-D3-dependent immune
340 activation at the onset of infection, indicating that B5-D3 acted not only as a receptor decoy but
341 also as an immune engager upon viral infection. Bio-distribution analysis of fluorescence-labeled
342 B5-D3 demonstrated rapid uptake and high accumulation in the respiratory tract, primarily
343 within airway macrophages. Phagocytosis assays further supported that sACE2-Fc decoy
344 mediated a rapid viral clearance in macrophages, while abolishing membrane ACE2-mediated
345 infection in epithelial cells. Together, these findings reveal a dual-function mechanism for
346 sACE2-Fc decoys in redirecting SARS-CoV-2 to phagocytic clearance and rapid immune
347 engagement, supporting their potential as intranasal prophylactics against respiratory viruses.

348 Previous studies have reported multiple ACE2 mutations with remarkable potential in
349 neutralizing SARS-CoV-2. However, in these studies, combining ACE2 mutations based on *in*
350 *silico* predictions to both enhance spike binding and eliminate the ACE2 enzymatic activity in a
351 single design resulted in accumulation of mutations such as K31F/N33D/H34S/E35Q/H345L
352 [12] and L79F/M82Y/Q325Y/H374A/H378A [14]. These extensive mutations have been
353 implicated in structural instability [12] and reduced production efficiency [17]. More importantly,
354 the high mutation loads raise risks for immunogenicity, which is a critical issue when considering
355 clinical applications. Corroboratively, Urano *et al.* detected *in vitro* T cell stimulation elicited by
356 the L79F mutation, whereas the T92Q mutation showed much lower immunogenicity and
357 enhanced spike binding affinity [45]. In our ACE2 decoy design, we incorporated only two
358 mutations (like T92Q and H374N in B5-D3) to enhance neutralization potency while eliminating
359 enzymatic activity, resulting in simplest compound ACE2 mutants. The B5-D3, as a
360 representative, exhibited not only minimal mutation-related risks but also top-level
361 neutralization potencies among all candidate mutants we tested. Hnece, by coupling structural
362 engineering (Fc fusion for avidity improvement) and mutagenesis (potency and safety
363 optimization), we provided simplest decoy design and further consolidated the generalizable
364 framework for decoy design, which is invaluable to combat a novel, highly contagious, and fatal
365 virus in future, before more effective vaccines and drugs are established.

366 Previous studies have reported that IN prophylaxis with sACE2-Fc mutants or monoclonal
367 antibodies [15, 16, 46] could effectively protect against SARS-CoV-2, in which the Fc-effector
368 functions were indispensable [14]. However, the precise mechanism has not been well depicted,
369 which prevents the further development of these approaches for translation. Here, our study
370 provided evidence for a deeper mechanistic insight, showing that IN sACE2-Fc decoys rapidly
371 engage host immunity in the respiratory tract. Consistently with others' work [14], IN delivery
372 of a Fc-null variant (B5-D3-LALA) resulted in suboptimal protection and higher viral infection

373 compared to B5-D3. Notably, despite the minimal infection observed, B5-D3-treated mice
374 showed robust early immune activation, including induction of antigen presentation and T cell
375 activation within 24 h post-infection (Fig 4). These results support that B5-D3 not only
376 neutralizes virus but also primes innate and adaptive immune responses, counteracting early-
377 stage viral immune evasion.

378 Furthermore, our bio-distribution data showed that IN-delivered B5-D3 preferentially
379 accumulates in the respiratory tract (Fig. 5a–d). Flow cytometry and confocal imaging confirmed
380 strong binding and uptake of B5-D3 by airway phagocytes, primarily alveolar macrophages and
381 monocyte-derived macrophages (Fig. 5e–l). Notably, phagocytosis assays demonstrated that B5-
382 D3–virus complexes were trafficked to lysosomes for degradation in macrophages. Functional
383 impairment in the B5-D3 structure reduced the uptake of virus by macrophages. These findings
384 support a mechanism in which B5-D3 redirects viral particles away from membrane ACE2-
385 dependent epithelial entry and toward phagocytic clearance (Fig. 7). Importantly, RNA-Seq
386 analysis of macrophages treated with virus-decoy complexes suggests that such ADCP-like
387 process also facilitated early immune activation and initiated downstream antiviral signaling
388 cascades before the virus reaches epithelial targets (Fig. 7b). Hence, the IN prophylaxis offers a
389 unique advantage by enabling localized immune priming and efficient viral clearance at the
390 frontline of infection. The IN-administered antibody drugs can share similar mechanism and
391 confer effective protection against primary infection of SARS-CoV-2 or other respiratory viruses.
392 However, antibody drugs can be easily escaped when new viral variants emerge, which is
393 specifically common among rapidly spreading respiratory RNA viruses [47]. In contrast, the
394 decoy strategy is intrinsically resistant to “antigenic escape” of the mutating virus, which is
395 further supported by the trend observed in viral evolution that later-emerging SARS-CoV-2
396 variants exhibit a higher affinity for the ACE2 receptor, enhancing their infectivity and
397 transmissibility [16].

398 In a post-infection context, respiratory viruses would have propagated extensively at the primary
399 infection site when symptoms arise, which makes IN neutralization relatively ineffective to clear
400 the high viral burden and the resultant systematic inflammation [48]. Therefore, the therapeutic
401 activity of either local or systemic neutralization at post-infection stage is bound to be restricted,
402 which is intrinsically inherited in all decoy/antibody therapies against respiratory viral infections.
403 Yet, transfusion of convalescent plasma or infusion of neutralizing mAbs in clinical practice have
404 been shown to reduce the mortality in COVID-19 [49, 50], and IV administration of B5-D3 as
405 therapy was also shown effective in improving the viral burden and survival in our aged mouse
406 experiment (Fig. 2a–e). Therefore, the therapeutic value of our decoy strategy does exist when a
407 "systematic" route of administration (*e.g.*, IV infusion) is chosen, and improvement in disease
408 severity should thus be expected.

409 Our study has several limitations. First, we didn't examine the potential of IgM-based sACE2
410 decamers, which showed higher avidity to spikes and greater potency for viral neutralization in
411 previous studies [46, 51, 52]. It is promising that our B5-D3 design would benefit from switching
412 to the IgM isotype, whereas the distinct biological features imposed by IgM Fc, including short
413 serum half-life and restricted tissue penetration [53], may complicate the analysis design and
414 diverge our study focus. Moreover, although no sign of B5-D3-specific immune responses was
415 observed in our AAV-injected mice, its immunogenicity and potential risk for antibody-
416 dependent enhancement (ADE) should be thoroughly evaluated to further develop the decoy
417 strategy for human use. Furthermore, despite that K18-hACE2 mice are broadly used and
418 demonstrate the best susceptibility to SARS-CoV-2 infection among established hACE2-
419 transgeic mouse models [54], hACE2 expression in these mice shows a distinct pattern that may
420 not reflect human physiology [31, 55]. Further study on hACE2 decoy using animals with
421 physiological level of hACE2 expression and humanized immune system that can support stable
422 engraftment of myeloid lineages would be warranted.

423 In conclusion, we present a rationally designed sACE2-Fc decoy with minimal mutagenesis (B5-
424 D3) and provide compelling evidence and insights into the immune mechanism supporting its
425 potent prophylactic efficacy. Intranasal prophylactic administration of B5-D3 not only
426 neutralizes SARS-CoV-2 but also redirects the virus toward phagocytic clearance, enabling early
427 immune engagement and complete protection. These findings provide a mechanistic basis for
428 decoy-based antiviral strategies and offer a promising approach to combat current and future
429 airborne viral threats. Further studies may aim to develop approaches to enhance the rapid local
430 immune engagement to restrict early viral propagation. Additionally, regimen refinements are
431 needed to enhance stability and functionality of decoy-based treatments before their clinical
432 translation and extension to a broader range of respiratory pathogens.

433

434 **MATERIALS AND METHODS**

435 **Plasmid construction**

436 The coding sequence of human ACE2 was cloned into the pGEM-T easy vector (Promega) and
437 underwent site-directed mutagenesis [10-12, 17]. The sACE2 and human IgG1 hinge-Fc regions
438 (aa 216-447) were assembled via overlapping PCR. These constructs, along with 6xHis-tagged
439 versions, were inserted into the HDM-SARS2-Spike-delta21 vector (Addgene #155130) to
440 generate HDM-CMV-sACE2(-Fc)-his plasmids. L234A/L235A (LALA) in hIgG1 were
441 introduced to generate HDM-CMV-sACE2-Fc-LALA-his plasmids. Various sACE2-Fc
442 fragments were then subcloned into pAAV-nEFCas9 vector (Addgene #87115) to generate AAV-
443 nEF-sACE2-Fc plasmids. SARS-CoV-2 spike variants with or without an HA tag fused to the C-
444 terminal were synthesized and inserted into the HDM vector [56].

445 **Protein structure visualization**

446 The crystal structure of SARS-CoV-2 spike receptor-binding domain bound with ACE2 (6M0J)

447 was downloaded from the Protein Data Bank (PDB, https://www.rcsb.org/structure/6m0j) [57].
448 Color-labeling of individual amino acids was performed on the PDB website. For structural
449 overlapping analysis of WT sACE2 and B5-D3 (aa 18-740), protein structures were predicted
450 using online AlphaFold 3 server (https://alphafoldserver.com/) [22]. PyMOL was utilized for root
451 mean square deviation (RMSD) calculations and structural visualization.

452 **Cell culture**

453 293T, Vero E6, Calu-3, and THP-1 cells were obtained from the American Type Culture
454 Collection and incubated at 37 °C with 5% CO_2. Specifically, 293T, Vero E6, and Calu-3 cells
455 were maintained in Dulbecco's Modified Eagle Medium (DMEM, Gibco) supplemented with
456 10% fetal bovine serum (FBS, Gibco) and 1% Penicillin-Streptomycin (PS, Gibco). THP-1 cells
457 were cultured in Roswell Park Memorial Institute 1640 medium (RPMI, Gibco) with similar
458 supplements. THP-1 cells were differentiated into M0 macrophages using 50 nM phorbol 12-
459 myristate 13-acetate (PMA) for 48 h, followed by a 24 h rest. For M1 macrophage differentiation,
460 post-PMA treatment cells were stimulated with 10 ng/mL lipopolysaccharide and 20 ng/mL
461 interferon (IFN)-γ for 24 h. Expi293 cells (Gibco) were cultured following the manufacturer's
462 instructions.

463 **Immunofluorescence staining of hACE2-293T and hACE2-Calu-3**

464 Cells were fixed, permeabilized, and blocked with 10% Normal Goat Serum (Invitrogen). ACE2
465 was stained with a primary antibody (Abcam #ab15348) followed by an Alexa Fluor 594-
466 conjugated secondary antibody (Invitrogen #A-21442). Cells were counterstained with Hoechst
467 33342 (Thermo Scientific) and examined under Nikon Ti2-E Inverted Fluorescence Microscope.

468 **Lentivirus packaging and transduction**

469 293T cells were seeded at 80% confluence and transfected with psPAX2 (Addgene #12260),
470 pMD2.G (Addgene #12259), and transfer plasmid pWPI-IRES-Puro-Ak-ACE2-TMPRSS2

471 (Addgene #154987) using polyethylenimine (PEI). Lentivirus-containing medium was harvested
472 72 h post-transfection, filtered through a 0.45 μM filter, concentrated, and stored at -80°C. For
473 transduction, 293T or Calu-3 cells were exposed to the concentrated lentivirus with 8 μg/mL
474 polybrene for 24 h to obtain human ACE2-overexpressing cell lines (hACE2-293T and hACE2-
475 Calu-3 respectively).

476 **Pseudovirus packaging, titration, and infection**

477 Pseudoviruses were packaged in 293T cells using pCDH-EF1a-eFFly-eGFP (Addgene #104834)
478 and spike-encoding plasmids, following a similar protocol to that of lentivirus. Post-packaging,
479 pseudoviral particles were titrated using the Lenti-X qRT-PCR Titration Kit (Takara #631235)
480 and used to infect target cells in the presence of 8 μg/mL polybrene. Infectivity was assessed via
481 a luciferase assay (Promega #E1501).

482 **Protein production and purification**

483 293T and Expi293 cells were transfected with HDM-CMV-sACE2(-Fc)(-LALA)-his plasmids
484 using PEI and ExpiFectamine 293 Transfection Kit (Gibco) respectively. Culture supernatants
485 were collected after 72 h and 5 days post-transfection respectively. The 293T supernatant was
486 assessed for ACE2 and IgG1 levels using enzyme-linked immunosorbent assay (ELISA) kits
487 (Abcam #ab235649; Invitrogen #BMS2092), and ACE2 activity was measured with a
488 fluorometric assay (Abcam # ab273297). The Expi293 supernatant underwent Ni-NTA Agarose
489 purification, followed by elution and buffer exchange to phosphate-buffered saline (PBS, pH
490 7.4). Protein concentration and integrity were verified using the Bradford method, ELISA, and
491 sodium dodecyl sulfate-polyacrylamide gel electrophoresis (SDS-PAGE).

492 ***In vitro* pseudovirus neutralization assay**

493 Conditioned media containing sACE2, sACE2-Fc or sACE2-Fc-LALA proteins were diluted
494 serially, mixed with pseudovirus (4×10^9 copies), and incubated at room temperature for 30

495 minutes [19]. The mixture was added to hACE2-293T cells in 96-well plates with duplicates
496 with 8 μg/mL polybrene. Transduction efficiency was assessed 48 h later via green fluorescent
497 protein (GFP) imaging and/or luciferase assays.

498 **Reporter-based *in vitro* ADCC and ADCP assays**

499 The *in vitro* antibody-dependent cell-mediated cytotoxicity (ADCC) and antibody-dependent
500 cellular phagocytosis (ADCP) activities of B5-D3(-LALA) were measured using Jurkat-Lucia
501 NFAT-CD16 and Jurkat-Lucia NFAT-CD32 cells (InvivoGen) respectively according to the
502 manufacturer's instructions. 293T cells transfected with pBOB-CAG-SARS-CoV-2-Spike-HA
503 (Addgene #141347) acted as target cells. Target cells were co-incubated with reporter cells and
504 serially diluted B5-D3(-LALA) at 37°C for 1 h. Luciferase expression indicating CD16 and
505 CD32 signaling was measured using QUANTI-Luc (InvivoGen).

506 **ADCP of pseudovirus** in THP-1 and THP-1-derived macrophages

507 SARS-CoV-2 pseudovirus (Wuhan-Hu-1, 8×10^8 copies in 10 μL) was mixed with 50 μL of B5-
508 D3 or control proteins (20 μg/mL) and added to THP-1, M0, or M1 cells cultured in a μSlide 18
509 Well iBITreat chamber slide. Here THP-1 cells were attached on the collagen-coated iBITreat
510 chamber slide. After 1, 3, 6, or 18 hours of incubation for phagocytosis, cells were fixed with
511 ice-cold methanol for 10 minutes, blocked with 10% normal goat serum for 1 hour at room
512 temperature, and immunostained sequentially for human IgG-Fc (Abcam #ab98596), HIV-1 p24
513 (Invitrogen #PA5-81773), and lysosomal associated membrane protein 1 (LAMP1) (Abcam
514 #ab25630). Secondary antibodies were applied (Invitrogen #A-21200 and #A-31573), and nuclei
515 were stained with Hoechst. Imaging was conducted using a Leica SP8 confocal microscope. p24
516 immunofluorescence intensity and colocalization with LAMP1 (Manders' coefficient) were
517 analyzed using ImageJ and the JACoP plugin.

518 For RNA extraction, M0 cells were washed once with PBS and added with TRIzol (Invitrogen)
519 after 6 h incubation with pseudovirus with/without B5-D3 (n = 3 in triplicate wells).

520 **Western blot for spike cleavage detection**

521 SARS-CoV-2 spike-HA tagged pseudovirus (4×10^9 copies) was incubated with M0/M1
522 macrophages or hACE2-293T cells for 6 h, with or without sACE2-Fc proteins. After incubation,
523 cell lysates were processed through SDS-PAGE and transferred to polyvinylidene difluoride
524 membranes. The membranes were blocked, incubated overnight with anti-HA (Merck Millipore
525 #05-904) and anti-β-actin (Santa Cruz #sc-47778) primary antibodies, then with horseradish
526 peroxidase (HRP)-conjugated secondary antibodies (Cell Signaling Technology #7076). Signals
527 were detected using the Amersham ECL select kit on a Bio-Rad ChemiDoc MP system.

528 **AAV vector packaging and purification**

529 As described previously [58], AAV vectors were produced in 293T cells transfected with AAV-
530 nEF-sACE2-Fc, pAdDeltaF6 (Addgene #112867), and pAAV2/8 (Addgene #112864) plasmids
531 using PEI. AAV particles were harvested from supernatants with Polyethylene Glycol (PEG)
532 8000 and from cell lysates via freeze-thaw cycles and benzonase digestion, then purified using
533 Iodixanol density gradient ultracentrifugation. AAV particles were concentrated and measured
534 using a qPCR AAV Titer Kit (Applied Biological Materials #G931).

535 **SARS-CoV-2 virus**

536 Experiments with live SARS-CoV-2 were performed at the BSL-3 core facility (LKS Faculty of
537 Medicine, HKU). The BetaCoV/Hong Kong/VM20001061/2020 virus, here regarded as the wild
538 type strain of SARS-CoV-2 (Wuhan-Hu-1), was isolated from the nasopharyngeal aspirate and
539 throat swab of a confirmed patient with COVID-19 in Hong Kong (GISAID identifier
540 EPI_ISL_412028). The SARS-CoV-2 variants were isolated from clinical specimens in Hong
541 Kong. Stock viruses were prepared with Vero E6 cells cultured in infection medium (DMEM

542 supplemented with 2% FBS and 1% PS).

543 **Median tissue culture infectious dose ($TCID_{50}$) assay**

544 Vero E6 cells pre-seeded in 96-well plates were infected with serially diluted virus stocks or
545 mouse lung homogenates in infection medium. After 72 h incubation, cytopathic effects (CPEs)
546 were observed under a microscope to calculate titers using the Reed–Muench method.

547 **Plaque-reduction neutralization test (PRNT) assay**

548 Casirivimab (#C100P) and hIgG1 isotype (clone 4F17, #PA007125) were purchased from Syd
549 Labs, USA) and used as controls. Purified B5-D3 and control proteins were serially diluted and
550 incubated with 50 PFU of SARS-CoV-2 (Wuhan-Hu-1, Delta, Omicron BA.5, BQ.1.22, and
551 XBB.1.5) for 1 h at room temperature, followed by addition to Vero E6 cells seeded in 6-well
552 plates. After incubation, cells were overlaid with agarose, fixed with formalin, and stained with
553 crystal violet. Plaque counts were used to calculate percentage neutralization and half maximal
554 inhibitory concentration (IC_{50}) values. The experiments were carried out in duplicates.

555 **Animal experiments**

556 The K18-hACE2 mice (B6.Cg-Tg(K18-ACE2)2Prlmn/J) [31] were purchased from the Jackson
557 Laboratory (Bar Harbor, ME, USA). Experiments on AAV or protein-only administration in mice
558 were carried out in the Animal Holding Core of the School of Biomedical Sciences, CUHK.
559 Experiments involving SARS-CoV-2 infection in K18-hACE2 mice were conducted within the
560 confines of the Biosafety Level 3 (BSL-3) core facility located at the Li Ka Shing Faculty of
561 Medicine, HKU. Experiments were conducted according to ethical practices to minimize animal
562 distress.

563 **AAV-mediated sACE2-Fc overexpression in mice**

564 Male K18-hACE2 mice [31] at the age of 2 months were injected intravenously with 1×10^{11}
565 GC of AAV-nEF-sACE2-Fc. Blood samples were collected periodically for analysis. Following

566 euthanasia, tissues were harvested for further DNA and histological analysis. sACE2-Fc
567 concentrations in sera and RAS metabolites were quantified using specific ELISA kits for Human
568 IgG1, Mouse Renin 1 (Invitrogen #EMREN1), Angiotensin II (LifeSpan BioSciences #LS-F523),
569 and Angiotensin 1-7 (LifeSpan BioSciences #LS-F40645).

570 **SARS-CoV-2 infection in mice**

571 Female K18-hACE2 mice, aged 10-12 months or 2-3 months, were intranasally inoculated with
572 1×10^4 plaque-forming unit (PFU) of SARS-CoV-2 Wuhan-Hu-1. Treatment with B5-D3 protein
573 was administered intranasally at 2.5 mg/kg or intravenously at 15 mg/kg, at various time points
574 relative to the viral challenge (6 h before, 24 h before, or 24 h after). Vehicle control groups
575 received PBS 6 h before viral challenge. Survival and weight were monitored daily for 14 days.
576 For the older mice, lung samples were collected from one mouse from each group at 4 days post-
577 infection (dpi) for analysis; younger mice had plasma collected for neutralizing antibody analysis
578 at 14 dpi. Another batch of young mice also received B5-D3(-LALA) protein pre-inoculation,
579 with lungs analyzed post-inoculation for RNA, viral load, and histopathology. A control group
580 of non-infected mice was used to assess baseline effects of B5-D3 on lung tissue.

581 **Neutralization assay for antibody titration**

582 Vero E6 cells were pre-seeded on 96-well plates 24 h before infection. On the day of infection,
583 the growth medium of the cells was changed to infection medium. The plasma samples were
584 serially 2-fold diluted with infection medium from a starting dilution of 1:10. The plasma was
585 then pre-incubated with 100 $TCID_{50}$ of SARS-CoV-2 for 1 h at room temperature before being
586 inoculated to the seeded Vero E6 cells in quadruplicates. At 72 h after inoculation, CPEs of the
587 cells were observed with optical microscopy. Neutralizing antibody titers against SARS-CoV-2
588 were expressed as the reciprocal of the highest dilution of plasma showing no CPEs in all 4 wells.
589 Uninfected cell monolayers were used as toxicity control.

590 **Histology**

591 Mouse tissues were fixed in 10% formalin, embedded in paraffin, and sectioned at 5 μm. Sections
592 of different organs were deparaffinized and underwent hematoxylin and eosin (H&E) staining.
593 For immunohistochemistry (IHC) staining, lung sections underwent antigen retrieval,
594 endogenous peroxidase blocking, and were incubated with primary antibodies against the SARS-
595 CoV/SARS-CoV-2 nucleocapsid protein (Sino Biological #40143-T62) overnight. After
596 washing, sections were stained with the anti-rabbit VECTASTAIN Elite ABC-HRP Kit (Vector
597 Laboratories), developed with 3,3′-Diaminobenzidine (Sigma #D4293), and counterstained with
598 Mayer's hematoxylin. Stained sections were scanned using Zeiss Axioscan 7 and analyzed using
599 ZEN (blue edition). For measurement of alveolar septal thickness, 10 fields from each lung H&E
600 section and 10 septa from each field were chosen for measurement using ImageJ.

601 **Quantitative PCR**

602 Quantitative PCR (qPCR) was used to analyze liver genomic DNA and lung RNA from mice.
603 DNA was extracted and qPCR was performed with the TB Green Premix Ex Taq II kit (Takara),
604 normalized to mouse *Gapdh* using the 2^-ΔCt method. RNA was extracted using TRIzol,
605 reverse-transcribed (Applied Biosystems #4368813), subjected to qPCR using the same kit and
606 normalized to mouse *Gapdh* levels. Specific primers are listed in Supplementary Table 2.

607 **RNA-Seq and data analysis**

608 Total RNA was extracted from mouse lung tissues or THP-1-derived M0 macrophages using
609 TRIzol and processed into transcriptome libraries with the TruSeq RNA Library Prep Kit
610 (illumina). Sequencing was performed on the NovaSeq 6000 or NovaSeq X Plus sequencers
611 (illumina) using a 150-base pair paired-end configuration. Sequencing data were processed with
612 fastp for quality control [59], then aligned to both the mouse (Ensembl GRCm39) and SARS-
613 CoV-2 (NCBI NC_045512v2) genomes using STAR [60] or to the human genome (Ensembl

614 GRCh38) using HISAT2 [61]. Pearson correlation and groupwise comparisons were conducted
615 in R: gene expression was quantified and analyzed for differential expression using DESeq2 [62];
616 up/downregulated gene enrichment and Gene Set Enrichment Analysis (GSEA) [63] was
617 performed using the clusterProfiler package [64].

618 **Tracking B5-D3 bio-distribution in mice**

619 B5-D3 were conjugated with Alexa Fluor 750 dye (B5-D3-AF750) as described [46]. In brief,
620 2 mg/mL solution of B5-D3 protein in 0.15 M $NaHCO_3$ was reacted with Alexa Fluor 750
621 succinimidyl ester (Thermo Fisher Scientific) at room temperature for 1 h. Unreacted dye was
622 removed by dialysis in PBS. All procedures were performed under dimmed light. Female K18-
623 hACE2 mice, aged 2-3 month, were administered intranasally with B5-D3-AF750 (2.5 mg/kg).
624 The mice were imaged at predetermined time points after administration (fluorescence ex = 745
625 nm, em = 800 nm, auto-exposure setting) using an IVIS Spectrum CT Imager (Perkin Elmer). At
626 the time of euthanasia, 50 μL of urine and blood, the brain, nasal cavity, trachea, lung, heart,
627 liver, spleen, kidney, and urinary bladder samples were excised and imaged. Regions of interest
628 (ROIs) were drawn, and average radiance ($p/s/cm^2/sr$) was measured. All images were processed
629 using Living Image software (Perkin Elmer) and the same fluorescence threshold was applied
630 for group comparison.

631 **Flow cytometry analysis and confocal microscopic imaging of BALF cells**

632 Mice were sacrificed via anesthetics overdose. Bronchoalveolar lavage was performed by
633 intratracheally rinsing the lungs with 1 mL of ice-cold Hanks' Balanced Salt Solution (HBSS,
634 Gibco) containing 100 μM ethylenediaminetetraacetic acid for four repeats. Bronchoalveolar
635 lavage fluid (BALF) was then centrifuged and treated with ammonium-chloride-potassium red
636 blood cell lysing buffer. For multicolor flow cytometry, cell pellets were washed with PBS and
637 stained with the Fixable Viability Stain 440UV dye (BD #566332). Next, the cells were blocked
638 with CD16/CD32 monoclonal antibody (Invitrogen #14-0161-85) and stained with antibodies

639 targeting the following molecules: CD45 (BD #568336), Siglec-F (BD #564514), CD11b (BD
640 #612800), CD11c (BD #751265), Ly6G (BD #563005), I-A/I-E major histocompatibility
641 complex class II (MHC-II) (BD #750171), F4/80 (BD #570288), Ly6C (BD #755198), and CD3
642 (BD #555275). Stained BALF cells were analyzed using the BD FACSymphony A5.2 SORP
643 Flow Cell Analyzer, and the results were analyzed using FlowJo v10.10.

644 For microscopic inspections, BALF cells were collected from mice, seeded in poly-d-lysine-
645 coated chamber slides and stained with antibodies targeting Siglec-F (BD #564514) and human
646 IgG-Fc (Abcam #ab98596). Secondary antibody (Invitrogen #A-11006) was applied. Stained
647 BALF cells were then counterstained with Hoechst and examined by confocal microscopy (Leica
648 TCS SP8).

649 **Statistical Analysis**

650 Assays including *in vitro* neutralization, PRNT, ADCC, and ADCP were conducted in technical
651 duplicates. Results were analyzed in GraphPad Prism version 9 using nonlinear regression to
652 calculate IC_{50} or half maximal effective concentration (EC_{50}) values. Transcriptomic analyses
653 were performed using R, with details provided in figure captions. All other statistical analyses
654 utilized GraphPad Prism version 9 with a significance threshold set at p value (p) < 0.05.

655

656 **SUPPLEMENTARY INFORMATION**

657 This PDF file includes:

658 Fig. S1 to S18; Tables S1 and S2.

659

660 **DECLARATIONS**

661 **Ethics approval and consent to participate**

All animal procedures were ethically approved by The Chinese University of Hong Kong (CUHK)'s Animal Experimentation Ethics Committee (approval number: 20-226-MIS) and The University of Hong Kong (HKU)'s Committee on the Use of Live Animals in Teaching and Research (approval number: 5511-20).

Availability of data and materials

All data associated with this study are available in the main text or the supplementary materials. The RNA-seq data generated in this study have been deposited in the NCBI Sequence Read Archive database under accession code PRJNA1054508. Constructs of diverse sACE2-Fc mutants and SARS-CoV-2 spikes are available upon request after completion and approval of a material transfer agreement by contacting fengbo@cuhk.edu.hk.

Competing interests

The authors declare that they have no competing interests.

Funding

This study was supported by Research Grants Council of Hong Kong grants 14115520, 14106024 (B.F.), C7145-20GF (L.L.P.), and in part by the Health@InnoHK Program launched by Innovation Technology Commission of the Hong Kong SAR, China. Jingyi W., J.L, B.L., and J.Q. received postgraduate studentships from the Chinese University of Hong Kong.

Authors' contributions

Jingyi W. and J.L. constructed the sACE2-Fc mutants and performed characterization analysis; A.W.C. performed the PRNTs and data analysis; Jingyi W., A.W.C., and J.L. performed the mouse infection experiments and data analysis; B.L., J.Q. and J.R. produced recombinant sACE2-Fc proteins; Jingyi W. and Junkang W. performed RNA-Seq analysis; Jingyi W. and J.Q. performed protein labeling, *in vivo* tracing of labeled protein, and flow cytometry analysis of BALF cells; J.L. performed THP-1 and Calu-3 experiments and confocal microscopic analysis.

686 Junkang W. and J.L. performed protein structure prediction and visualization. Jingyi W., J.L.,
687 L.L.P. and B.F. conceived the project, designed experiments, and wrote the manuscript. Y.X.,
688 T.B., L.L.P. and B.F. revised the manuscript. All authors read and approved the final manuscript.

689 **Acknowledgements**

690 We thank the Chinese University of Hong Kong (CUHK) and the University of Hong Kong
691 (HKU) research platforms for assistance in animal experimentation (the Laboratory Animal
692 Service Center at CUHK and the Centre for Comparative Medicine Research at HKU) and
693 histological analysis (Department of Pathology, HKU and Core Laboratory in the School of
694 Biomedical Sciences, CUHK).

695

696 **REFERENCES**

697 [1] Q. Wang *et al.*, "Alarming antibody evasion properties of rising SARS-CoV-2 BQ and XBB subvariants,"
698 *Cell,* vol. 186, no. 2, pp. 279-286.e8, 2023, doi: 10.1016/j.cell.2022.12.018.
699 [2] M. Hoffmann *et al.*, "SARS-CoV-2 Cell Entry Depends on ACE2 and TMPRSS2 and Is Blocked by a
700 Clinically Proven Protease Inhibitor," *Cell,* vol. 181, no. 2, pp. 271-280.e8, 2020/04/16/ 2020, doi:
701 https://doi.org/10.1016/j.cell.2020.02.052.
702 [3] S. Ozono *et al.*, "SARS-CoV-2 D614G spike mutation increases entry efficiency with enhanced ACE2-
703 binding affinity," *Nature Communications,* vol. 12, no. 1, p. 848, 2021/02/08 2021, doi: 10.1038/s41467-
704 021-21118-2.
705 [4] M. Ramanathan, I. D. Ferguson, W. Miao, and P. A. Khavari, "SARS-CoV-2 B.1.1.7 and B.1.351 spike
706 variants bind human ACE2 with increased affinity," *The Lancet Infectious Diseases,* vol. 21, no. 8, p. 1070,
707 2021, doi: 10.1016/S1473-3099(21)00262-0.
708 [5] L. Li *et al.*, "Structural basis of human ACE2 higher binding affinity to currently circulating Omicron
709 SARS-CoV-2 sub-variants BA.2 and BA.1.1," *Cell,* vol. 185, no. 16, pp. 2952-2960.e10, 2022, doi:
710 10.1016/j.cell.2022.06.023.
711 [6] V. Monteil *et al.*, "Inhibition of SARS-CoV-2 Infections in Engineered Human Tissues Using Clinical-
712 Grade Soluble Human ACE2," *Cell,* vol. 181, no. 4, pp. 905-913.e7, 2020/05/14/ 2020, doi:
713 https://doi.org/10.1016/j.cell.2020.04.004.
714 [7] A. Zoufaly *et al.*, "Human recombinant soluble ACE2 in severe COVID-19," *The Lancet Respiratory*
715 *Medicine,* vol. 8, no. 11, pp. 1154-1158, 2020, doi: 10.1016/S2213-2600(20)30418-5.
716 [8] R. A. S. Santos *et al.*, "The ACE2/Angiotensin-(1-7)/MAS Axis of the Renin-Angiotensin System: Focus
717 on Angiotensin-(1-7)," *Physiol Rev,* vol. 98, no. 1, pp. 505-553, Jan 1 2018, doi:
718 10.1152/physrev.00023.2016.
719 [9] P. Liu *et al.*, "Novel ACE2-Fc chimeric fusion provides long-lasting hypertension control and organ
720 protection in mouse models of systemic renin angiotensin system activation," *Kidney International,* vol.
721 94, no. 1, pp. 114-125, 2018/07/01/ 2018, doi: https://doi.org/10.1016/j.kint.2018.01.029.

[10] Z. Payandeh *et al.*, "Design of an engineered ACE2 as a novel therapeutics against COVID-19," *Journal of Theoretical Biology,* vol. 505, p. 110425, 2020/11/21/ 2020, doi: https://doi.org/10.1016/j.jtbi.2020.110425.

[11] C. Lei *et al.*, "Neutralization of SARS-CoV-2 spike pseudotyped virus by recombinant ACE2-Ig," *Nature Communications,* vol. 11, no. 1, p. 2070, 2020/04/24 2020, doi: 10.1038/s41467-020-16048-4.

[12] A. Glasgow *et al.*, "Engineered ACE2 receptor traps potently neutralize SARS-CoV-2," *Proceedings of the National Academy of Sciences,* vol. 117, no. 45, pp. 28046-28055, 2020, doi: 10.1073/pnas.2016093117.

[13] P. Liu, X. Xie, L. Gao, and J. Jin, "Designed variants of ACE2-Fc that decouple anti-SARS-CoV-2 activities from unwanted cardiovascular effects," *Int J Biol Macromol,* vol. 165, no. Pt B, pp. 1626-1633, Dec 15 2020, doi: 10.1016/j.ijbiomac.2020.10.120.

[14] Y. Chen *et al.*, "Engineered ACE2-Fc counters murine lethal SARS-CoV-2 infection through direct neutralization and Fc-effector activities," *Science Advances,* vol. 8, no. 28, p. eabn4188, 2022, doi: doi:10.1126/sciadv.abn4188.

[15] L. Hassler *et al.*, "Intranasal soluble ACE2 improves survival and prevents brain SARS-CoV-2 infection," *Life Science Alliance,* vol. 6, no. 7, p. e202301969, 2023, doi: 10.26508/lsa.202301969.

[16] D. L. Kober *et al.*, "Development of a mutant aerosolized ACE2 that neutralizes SARS-CoV-2 *in vivo*," *mBio,* vol. 15, no. 6, pp. e00768-24, 2024, doi: doi:10.1128/mbio.00768-24.

[17] K. K. Chan *et al.*, "Engineering human ACE2 to optimize binding to the spike protein of SARS coronavirus 2," *Science,* vol. 369, no. 6508, pp. 1261-1265, 2020, doi: 10.1126/science.abc0870.

[18] J. L. Guy, R. M. Jackson, H. A. Jensen, N. M. Hooper, and A. J. Turner, "Identification of critical active-site residues in angiotensin-converting enzyme-2 (ACE2) by site-directed mutagenesis," *The FEBS Journal,* vol. 272, no. 14, pp. 3512-3520, 2005, doi: https://doi.org/10.1111/j.1742-4658.2005.04756.x.

[19] K. H. D. Crawford *et al.*, "Protocol and Reagents for Pseudotyping Lentiviral Particles with SARS-CoV-2 Spike Protein for Neutralization Assays," *Viruses,* vol. 12, no. 5, p. 513, 2020. [Online]. Available: https://www.mdpi.com/1999-4915/12/5/513.

[20] B. Korber *et al.*, "Tracking Changes in SARS-CoV-2 Spike: Evidence that D614G Increases Infectivity of the COVID-19 Virus," *Cell,* vol. 182, no. 4, pp. 812-827.e19, 2020/08/20/ 2020, doi: https://doi.org/10.1016/j.cell.2020.06.043.

[21] K. Suryamohan *et al.*, "Human ACE2 receptor polymorphisms and altered susceptibility to SARS-CoV-2," *Communications Biology,* vol. 4, no. 1, p. 475, 2021/04/12 2021, doi: 10.1038/s42003-021-02030-3.

[22] J. Abramson *et al.*, "Accurate structure prediction of biomolecular interactions with AlphaFold 3," *Nature,* vol. 630, no. 8016, pp. 493-500, 2024/06/01 2024, doi: 10.1038/s41586-024-07487-w.

[23] W. F. Garcia-Beltran *et al.*, "Multiple SARS-CoV-2 variants escape neutralization by vaccine-induced humoral immunity," *Cell,* vol. 184, no. 9, pp. 2372-2383.e9, 2021, doi: 10.1016/j.cell.2021.03.013.

[24] P. Mlcochova *et al.*, "SARS-CoV-2 B.1.617.2 Delta variant replication and immune evasion," *Nature,* vol. 599, no. 7883, pp. 114-119, 2021/11/01 2021, doi: 10.1038/s41586-021-03944-y.

[25] I. Kimura *et al.*, "The SARS-CoV-2 Lambda variant exhibits enhanced infectivity and immune resistance," *Cell Reports,* vol. 38, no. 2, p. 110218, 2022/01/11/ 2022, doi: https://doi.org/10.1016/j.celrep.2021.110218.

[26] P. J. Halfmann *et al.*, "Characterization of the SARS-CoV-2 B.1.621 (Mu) variant," *Science Translational Medicine,* vol. 14, no. 657, p. eabm4908, 2022, doi: doi:10.1126/scitranslmed.abm4908.

[27] Y. Cao *et al.*, "Omicron escapes the majority of existing SARS-CoV-2 neutralizing antibodies," *Nature,* vol. 602, no. 7898, pp. 657-663, 2022/02/01 2022, doi: 10.1038/s41586-021-04385-3.

[28] S. Wang *et al.*, "Genomic Surveillance for SARS-CoV-2 - China, September 26, 2022 to January 29, 2023," (in eng), *China CDC weekly,* vol. 5, no. 7, pp. 143-151, Feb 17 2023, doi: 10.46234/ccdcw2023.026.

[29] R. Amin, P. Pal, K. Dhama, and T. B. Emran, "Recent update on XBB.1.5 emerging novel mutation of

COVID-19," *International Journal of Surgery,* vol. 109, no. 4, pp. 1048-1049, 2023, doi: 10.1097/js9.0000000000000254.

[30] D. M. Weinreich *et al.*, "REGEN-COV Antibody Combination and Outcomes in Outpatients with Covid-19," *New England Journal of Medicine,* vol. 385, no. 23, p. e81, 2021, doi: 10.1056/NEJMoa2108163.

[31] P. B. McCray *et al.*, "Lethal Infection of K18-*hACE2* Mice Infected with Severe Acute Respiratory Syndrome Coronavirus," *Journal of Virology,* vol. 81, no. 2, pp. 813-821, 2007, doi: doi:10.1128/JVI.02012-06.

[32] V. Dwivedi *et al.*, "Age associated susceptibility to SARS-CoV-2 infection in the K18-hACE2 transgenic mouse model," *Geroscience,* vol. 46, no. 3, pp. 2901-2913, Jun 2024, doi: 10.1007/s11357-024-01102-6.

[33] J. Lund *et al.*, "Human Fc gamma RI and Fc gamma RII interact with distinct but overlapping sites on human IgG," *The Journal of Immunology,* vol. 147, no. 8, pp. 2657-2662, 1991, doi: 10.4049/jimmunol.147.8.2657.

[34] E. S. Winkler *et al.*, "SARS-CoV-2 infection of human ACE2-transgenic mice causes severe lung inflammation and impaired function," *Nature Immunology,* vol. 21, no. 11, pp. 1327-1335, 2020/11/01 2020, doi: 10.1038/s41590-020-0778-2.

[35] Q. Shan *et al.*, "Tcf1 and Lef1 provide constant supervision to mature CD8+ T cell identity and function by organizing genomic architecture," *Nature Communications,* vol. 12, no. 1, p. 5863, 2021/10/06 2021, doi: 10.1038/s41467-021-26159-1.

[36] Y. Yamakita *et al.*, "Fascin1 Promotes Cell Migration of Mature Dendritic Cells," *The Journal of Immunology,* vol. 186, no. 5, pp. 2850-2859, 2011, doi: 10.4049/jimmunol.1001667.

[37] M. Colomer-Molera *et al.*, "Kv1.3-dependent immune system activation is regulated by KCNE4," *Biophysical Journal,* vol. 122, no. 3, p. 14a, 2023, doi: 10.1016/j.bpj.2022.11.302.

[38] M. Rapp *et al.*, "CCL22 controls immunity by promoting regulatory T cell communication with dendritic cells in lymph nodes," *Journal of Experimental Medicine,* vol. 216, no. 5, pp. 1170-1181, 2019, doi: 10.1084/jem.20170277.

[39] Z. R. Korobova, N. A. Arsentieva, and A. A. Totolian, "Macrophage-Derived Chemokine MDC/CCL22: An Ambiguous Finding in COVID-19," *International Journal of Molecular Sciences,* vol. 24, no. 17, p. 13083, 2023. [Online]. Available: https://www.mdpi.com/1422-0067/24/17/13083.

[40] K. Katagiri, M. Hattori, N. Minato, and T. Kinashi, "Rap1 Functions as a Key Regulator of T-Cell and Antigen-Presenting Cell Interactions and Modulates T-Cell Responses," *Molecular and Cellular Biology,* vol. 22, no. 4, pp. 1001-1015, 2002/02/01 2002, doi: 10.1128/MCB.22.4.1001-1015.2002.

[41] W. Chanput, J. J. Mes, and H. J. Wichers, "THP-1 cell line: An in vitro cell model for immune modulation approach," *International Immunopharmacology,* vol. 23, no. 1, pp. 37-45, 2014/11/01/ 2014, doi: https://doi.org/10.1016/j.intimp.2014.08.002.

[42] S. Tedesco *et al.*, "Convenience versus Biological Significance: Are PMA-Differentiated THP-1 Cells a Reliable Substitute for Blood-Derived Macrophages When Studying in Vitro Polarization?," (in English), *Frontiers in Pharmacology,* Original Research vol. 9, 2018-February-22 2018, doi: 10.3389/fphar.2018.00071.

[43] K. Takeda and S. Akira, "Toll-like receptors in innate immunity," *International Immunology,* vol. 17, no. 1, pp. 1-14, 2005, doi: 10.1093/intimm/dxh186.

[44] S. Yu *et al.*, "SARS-CoV-2 spike engagement of ACE2 primes S2′ site cleavage and fusion initiation," *Proceedings of the National Academy of Sciences,* vol. 119, no. 1, p. e2111199119, 2022, doi: doi:10.1073/pnas.2111199119.

[45] E. Urano *et al.*, "An inhaled ACE2 decoy confers protection against SARS-CoV-2 infection in preclinical models," *Science Translational Medicine,* vol. 15, no. 711, p. eadi2623, 2023, doi:

doi:10.1126/scitranslmed.adi2623.

[46] Z. Ku *et al.*, "Nasal delivery of an IgM offers broad protection from SARS-CoV-2 variants," *Nature,* vol. 595, no. 7869, pp. 718-723, 2021/07/01 2021, doi: 10.1038/s41586-021-03673-2.

[47] A. M. Carabelli *et al.*, "SARS-CoV-2 variant biology: immune escape, transmission and fitness," *Nature Reviews Microbiology,* vol. 21, no. 3, pp. 162-177, 2023/03/01 2023, doi: 10.1038/s41579-022-00841-7.

[48] N. R. Cheemarla *et al.*, "Dynamic innate immune response determines susceptibility to SARS-CoV-2 infection and early replication kinetics," *Journal of Experimental Medicine,* vol. 218, no. 8, 2021, doi: 10.1084/jem.20210583.

[49] J. W. Senefeld *et al.*, "COVID-19 Convalescent Plasma for the Treatment of Immunocompromised Patients: A Systematic Review and Meta-analysis," *JAMA Network Open,* vol. 6, no. 1, pp. e2250647-e2250647, 2023, doi: 10.1001/jamanetworkopen.2022.50647.

[50] A. Gupta *et al.*, "Early Treatment for Covid-19 with SARS-CoV-2 Neutralizing Antibody Sotrovimab," *New England Journal of Medicine,* vol. 385, no. 21, pp. 1941-1950, 2021, doi: doi:10.1056/NEJMoa2107934.

[51] J. Liu *et al.*, "An IgM-like inhalable ACE2 fusion protein broadly neutralizes SARS-CoV-2 variants," *Nat Commun,* vol. 14, no. 1, p. 5191, Aug 25 2023, doi: 10.1038/s41467-023-40933-3.

[52] H. Guo *et al.*, "An ACE2 decamer viral trap as a durable intervention solution for current and future SARS-CoV," *Emerging Microbes & Infections,* vol. 12, no. 2, p. 2275598, 2023/12/08 2023, doi: 10.1080/22221751.2023.2275598.

[53] B. A. Keyt, R. Baliga, A. M. Sinclair, S. F. Carroll, and M. S. Peterson, "Structure, Function, and Therapeutic Use of IgM Antibodies," *Antibodies,* vol. 9, no. 4, p. 53, 2020. [Online]. Available: https://www.mdpi.com/2073-4468/9/4/53.

[54] C. Lutz, L. Maher, C. Lee, and W. Kang, "COVID-19 preclinical models: human angiotensin-converting enzyme 2 transgenic mice," *Hum Genomics,* vol. 14, no. 1, p. 20, Jun 4 2020, doi: 10.1186/s40246-020-00272-6.

[55] F. S. Oladunni *et al.*, "Lethality of SARS-CoV-2 infection in K18 human angiotensin-converting enzyme 2 transgenic mice," *Nat Commun,* vol. 11, no. 1, p. 6122, Nov 30 2020, doi: 10.1038/s41467-020-19891-7.

[56] Y. Shu and J. McCauley, "GISAID: Global initiative on sharing all influenza data – from vision to reality," *Eurosurveillance,* vol. 22, no. 13, p. 30494, 2017, doi: doi:https://doi.org/10.2807/1560-7917.ES.2017.22.13.30494.

[57] J. Lan *et al.*, "Structure of the SARS-CoV-2 spike receptor-binding domain bound to the ACE2 receptor," *Nature,* vol. 581, no. 7807, pp. 215-220, 2020/05/01 2020, doi: 10.1038/s41586-020-2180-5.

[58] X. He *et al.*, "Low-dose AAV-CRISPR-mediated liver-specific knock-in restored hemostasis in neonatal hemophilia B mice with subtle antibody response," *Nature Communications,* vol. 13, no. 1, p. 7275, 2022/11/25 2022, doi: 10.1038/s41467-022-34898-y.

[59] S. Chen, Y. Zhou, Y. Chen, and J. Gu, "fastp: an ultra-fast all-in-one FASTQ preprocessor," *Bioinformatics,* vol. 34, no. 17, pp. i884-i890, 2018, doi: 10.1093/bioinformatics/bty560.

[60] N. D. Maulding, S. Seiler, A. Pearson, N. Kreusser, and J. M. Stuart, "Dual RNA-Seq analysis of SARS-CoV-2 correlates specific human transcriptional response pathways directly to viral expression," *Scientific Reports,* vol. 12, no. 1, p. 1329, 2022/01/25 2022, doi: 10.1038/s41598-022-05342-4.

[61] D. Kim, J. M. Paggi, C. Park, C. Bennett, and S. L. Salzberg, "Graph-based genome alignment and genotyping with HISAT2 and HISAT-genotype," *Nature Biotechnology,* vol. 37, no. 8, pp. 907-915, 2019/08/01 2019, doi: 10.1038/s41587-019-0201-4.

[62] M. I. Love, W. Huber, and S. Anders, "Moderated estimation of fold change and dispersion for RNA-seq

data with DESeq2," *Genome Biology,* vol. 15, no. 12, p. 550, 2014/12/05 2014, doi: 10.1186/s13059-014-0550-8.

[63] A. Subramanian *et al.*, "Gene set enrichment analysis: A knowledge-based approach for interpreting genome-wide expression profiles," *Proceedings of the National Academy of Sciences,* vol. 102, no. 43, pp. 15545-15550, 2005, doi: doi:10.1073/pnas.0506580102.

[64] T. Wu *et al.*, "clusterProfiler 4.0: A universal enrichment tool for interpreting omics data," *The Innovation,* vol. 2, no. 3, p. 100141, 2021/08/28/ 2021, doi: https://doi.org/10.1016/j.xinn.2021.100141.

FIGURE LEGENDS

Fig. 1 Enhanced sACE2-Fc with two single mutations exhibited broad-spectrum neutralization of SARS-CoV-2 variants. a Schematic representation of sACE2-Fc structure (upper) and neutralization assay setup (lower). Key amino acid positions (90-92 and 374-378) involved in glycosylation and zinc binding are highlighted. Red stars mark the positions of mutations in the sACE2-Fc mutant B5-D3. SP, signal peptide; CLD, collectrin-like domain; hIgG1, human IgG1. **b** Comparative bar graph showing the half-maximal inhibitory concentration (IC_{50}) values for neutralization of Wuhan-Hu-1 and D614G pseudovirues by WT sACE2-Fc and mutants (B2 to B6, A2, A3, D1 to D5, and B5-derivatives). The red arrow emphasizes the superior performance of the B5-D3 mutant. Enzymatic activity of each construct is plotted on the right axis. **c** List of pseudoviruses carrying spikes from different SARS-CoV-2 variants tested, categorized by the World Health Organization (WHO) into VOCs and VOIs. **d** Graph displaying IC_{50} values of WT sACE2-Fc, B5, and B5-D3/4/5 mutants against various SARS-CoV-2 VOCs and VOIs in neutralization assays. **e** Schematics of the plaque-reduction neutralization tests (PRNTs) process (upper) and the resulting IC_{50} values for B5-D3, Casirivimab, and hIgG1 against authentic SARS-CoV-2 (lower). **f, g** Dose-response curves depicting the neutralization efficacy of B5-D3 (orange), Casirivimab (purple), and hIgG1 (grey) in PRNTs against authentic SARS-CoV-2 Wuhan-Hu-1 and Delta strains (**f**), and Omicron sub-lineages (**g**). Data are presented as mean ± standard deviation (SD) from duplicate experiments.

885

886 **Fig. 2 Enhanced survival and reduced infection in K18-hACE2 mice through intranasal**
887 **prophylaxis with B5-D3 against SARS-CoV-2. a–e** Female K18-hACE2 mice, aged 10 to 12
888 months, were inoculated with 1×10^4 PFU of SARS-CoV-2 (Wuhan-Hu-1 strain). Mice were
889 treated with B5-D3 6 h prior (–6 h) via intranasal (IN, red) or intravenous (IV, green) routes, or
890 24 h post-infection (+24 h, blue) via IV (n = 4 + 1). IN PBS administered 6 h prior to viral
891 challenge served as the vehicle control (black; n = 4 + 1), and PBS alone was used for mock
892 control (grey; n = 3 + 1) (**a**). Body weight and survival (n = 3 or 4) were monitored over 14 days
893 (**b**, **c**). One mouse from each group was sacrificed at 4 dpi for analysis of viral titers in lung
894 homogenates using a median tissue culture infectious dose ($TCID_{50}$) assay (**d**) and histological
895 analysis of lung sections (upper, IHC staining for N protein; lower, H&E staining) (**e**). Black
896 arrows indicate alveolar thickening, and yellow arrows show leukocyte infiltration. Scale bar =
897 100 μm. ND, not detected; LOD, limit of detection. **f–i** Young female K18-hACE2 mice, aged 2
898 to 3 months, were inoculated similarly and treated with B5-D3 via IN route at 24 h before (–24
899 h, pink), 6 h before (–6 h, red), or 24 h after (+24 h, orange) the viral challenge (n = 5). Mice
900 receiving IN PBS 6 h before infection served as the vehicle control (black), with mock control
901 mice receiving PBS alone (grey) (**f**). Body weight (**g**) and survival (**h**) were recorded for 14 days.
902 Neutralizing antibody titers against Wuhan-Hu-1 in serum samples from surviving mice at 14
903 dpi were determined using Vero E6 cells (**i**). nAb, neutralizing antibody. Data are presented as
904 the geometric mean ± geometric SD. Statistical significance was determined using Dunn's
905 multiple comparisons test.

906

907 **Fig. 3 Efficient viral clearance at early stages through intranasal prophylaxis with B5-D3**
908 **against SARS-CoV-2 challenge in K18-hACE2 mice. a** Workflow diagram showing timelines
909 and treatments for different mouse groups. Young female K18-hACE2 mice aged 2 to 3 months
910 received prophylactic administration of PBS (black), B5-D3 (red), or B5-D3-LALA (purple) via
911 the IN route 6 h prior to inoculation with 1×10^4 PFU of Wuhan-Hu-1. Mice inoculated with
912 PBS instead of the virus served as mock controls (grey). Mice from each treatment group were
913 sacrificed for tissue collection at 1, 2, and 4 dpi ($n = 3$ per time point). **b** Quantitative PCR results
914 showing relative amounts of *S* (upper) and *N* (lower) viral RNA in lung tissues collected from
915 different groups at 1, 2, and 4 dpi, normalized to mouse *Gapdh*. **c** The titers of infectious viruses
916 detected in lung homogenates, measured by $TCID_{50}$ assays at 1, 2, and 4 dpi. **d, e** Fixed lung
917 tissues were sectioned and stained; IHC for viral N protein (**d**) and H&E staining for tissue
918 damage (**e**) are shown (scale bar = 100 μm). Data presented as mean ± standard error of the mean
919 (SEM). Statistical significance was determined by Tukey's multiple comparisons test.
920
921
922 **Fig. 4 Transcriptomic analysis of lungs revealed early immune activation in IN B5-D3-**
923 **prophylaxis mouse group after SARS-CoV-2 challenge. a–d** DGE analysis comparing PBS
924 (**a**), B5-D3 (**c**), and B5-D3-LALA (**d**) against the mock control at specific time points ($n = 3$).
925 Volcano plots illustrate the gene expression changes (**a**, **c**, **d**), while red and blue dots represent
926 significantly upregulated and downregulated genes, respectively, with $|\log_2$ fold change
927 $(\log_2 FC)| \geq 1$ and a false discovery rate (FDR) < 0.05. Bar chart in **b** shows the enrichment of
928 GOBP "response to virus" observed in PBS groups at 1, 2, 4 dpi, in which adjusted *p* values are
929 indicated for individual comparisons. **e–g** Comparison between IN B5-D3 and PBS group at 1
930 dpi. Volcano plot illustrates the DGE analysis between IN B5-D3 to PBS group at 1 dpi (**e**), with

red and blue dots representing significantly upregulated and downregulated genes, respectively, with $|\log_2 FC| \geq 1$ and FDR < 0.05. GSEA shows top 15 significantly activated GOBPs (**f**) and KEGG pathways (**g**) in IN B5-D3 compared to PBS group at 1 dpi. NES, normalized enrichment score; p.adj, adjusted *p* value. **h**–**j** GSEA plots of chemotaxis (**h**), Rap1 signaling pathway (**i**), and Th1 and Th2 cell differentiation (**j**) in B5-D3 vs PBS comparison at 1 dpi. **k**, **l** Heatmaps show NES of GSEA comparing various treatments to the mock control (**k**) and between B5-D3 to PBS (**l**), focusing on top 10 GOBPs in **f** and **Supplementary Fig. 10c, d**, respectively, and those related to immune cell chemotaxis. Significant NES values ($p < 0.05$, FDR < 0.25) are highlighted in yellow. Purple boxes indicate GOBPs where B5-D3 (1 dpi) group shows activation but PBS (1 dpi) group shows suppression. Benjamin–Hochberg method was used for FDR adjustment.

Fig. 5 *In vivo* bio-distribution of B5-D3 after IN administration. a Schematic workflow of *in vivo* and *ex vivo* imaging. Female K18-hACE2 mice aged 2 to 3 months received IN administration of fluorescently labeled B5-D3 (B5-D3-AF750) and was visualized at different time points. **b** Representative whole-body images of control and treated mice at 5 min, 1 h, and 24 h after B5-D3-AF750 administration, showing the signal captured by *in vivo* imaging (left). White circles indicate regions of interest (ROIs) for quantification of fluorescence signals in the nasal cavities. Average (Avg) Radiance measured at all time points are shown on the right. **c** *Ex vivo* images of tissues from control and treated mice sacrificed at indicated time points after B5-D3-AF750 administration. Blue circles indicate ROIs for signal quantification. Br, brain; NC, nasal cavity; T, trachea; Lu, lung; H, heart; Lv, liver; S, spleen; K, kidney; UB, urinary bladder; Bl, blood; Ur, urine. **d** Avg Radiance shows the fluorescence signals in excised tissues measured *ex vivo*. **e** Schematic workflow for BALF analysis. Female K18-hACE2 mice aged 2 to 3 months received IN administration of B5-D3-AF750 ($n = 3$) or PBS ($n = 4$) and were sacrificed at 6 h later for collection of BALF cells. **f** Percentage of $CD45^+$ cells in live BALF cells. **g** Positive

957 rates (left) and histograms (right) of B5-D3 binding/uptake in $CD45^+$ BALF cells. Histograms
958 show B5-D3-AF750 fluorescence intensities in $CD45^+$ BALF cells from individual mice. **h**
959 Frequency of individual immune cell types in $CD45^+B5\text{-}D3^+$ BALF cells. Red arrows point out
960 AMs and mono-Macs with high abundance. AM, alveolar macrophage; Mono-Mac, monocyte-
961 derived macrophage; cDC1/2, type 1 or 2 conventional dendritic cells. **i**, **j** Positive rates (left)
962 and histograms (right) of B5-D3 binding/uptake in $CD11c^+$Siglec-F^+ AMs (**i**) and $CD11b^-F4/80^+$
963 mono-Macs (**j**). **k** Median fluorescence intensity (MFI) of AF750 indicates B5-D3
964 binding/uptake in different $CD45^+B5\text{-}D3^+$ populations. **l** Confocal images (scale bar = 50 μm)
965 of BALF cells collected at 6 h and stained for sACE2-Fc (red, anti-Fc, Abcam #ab98596), Siglec-
966 F (green, BD #564514), and nuclei (blue, Hoechst). Magnified views are shown in white
967 rectangles. Data are presented as mean ± SEM, and statistical significance was determined by
968 Tukey's multiple comparisons test or Student's t-test.

969

970 **Fig. 6 B5-D3 enhanced phagocytosis and degradation of SARS-CoV-2 pseudovirus in THP-**
971 **1-derived macrophages. a** Immunostaining of p24 (Invitrogen #PA5-81773), sACE2-Fc, and
972 LAMP1 (Abcam #ab25630) in THP-1-differentiated M0 macrophages showing phagocytosis of
973 SARS-CoV-2 pseudovirus (PV, $p24^+$) after 6 h of incubation with or without B5-D3 (scale bar =
974 50 μm). LAMP1 was stained to identify lysosomes. **b** Quantification of p24 signal intensity as
975 shown in **a**. Intensity Density (IntDen) per cell number indicates the mean p24 signal per cell,
976 calculated using ImageJ. Each dot represents one image. **c** Manders' coefficient indicating the
977 colocalization of p24 and LAMP1 in THP-1 M0 macrophages as shown in **a**. **d** Immunostaining
978 of p24, sACE2-Fc, and LAMP1 in hACE2-Calu-3 cells after 6 h incubation with pseudovirus,
979 with or without B5-D3 (scale bar = 50 μm). **e** Quantification of mean p24 signal intensity as
980 shown in **d**. **f** Manders' coefficient for the colocalization of p24 and LAMP1 in hACE2-Calu-3
981 cells, as shown in **d**. **g** Quantification of pseudovirus infection in THP-1, M0 macrophages, M1

macrophages, hACE2-Calu-3, and hACE2-293T cells, in the presence or absence of B5-D3. Results shown are luciferase activities measured at 2 days post-transduction. **h** Immunoblot staining of cell lysates to detect SARS-CoV-2 spike cleavage after cell entry. M0 macrophages, M1 macrophages, and hACE2-293T cells were incubated with pseudovirus for 6 h, with or without B5-D3, before protein extraction. Band locations of SARS-CoV-2 spike S2 and S2′ fragments are labeled in black and red respectively. Data are presented as mean ± SEM, and statistical significance was determined by Tukey's multiple comparisons test.

Fig. 7 Proposed mechanisms of action of IN sACE2-Fc decoy in preventing SARS-CoV-2 infection. a, b Schematics illustrating the actions and outcomes of SARS-CoV-2 infection, in the absence (**a**) and presence (**b**) of IN delivered sACE2-Fc decoys. The figure was generated in Biorender.

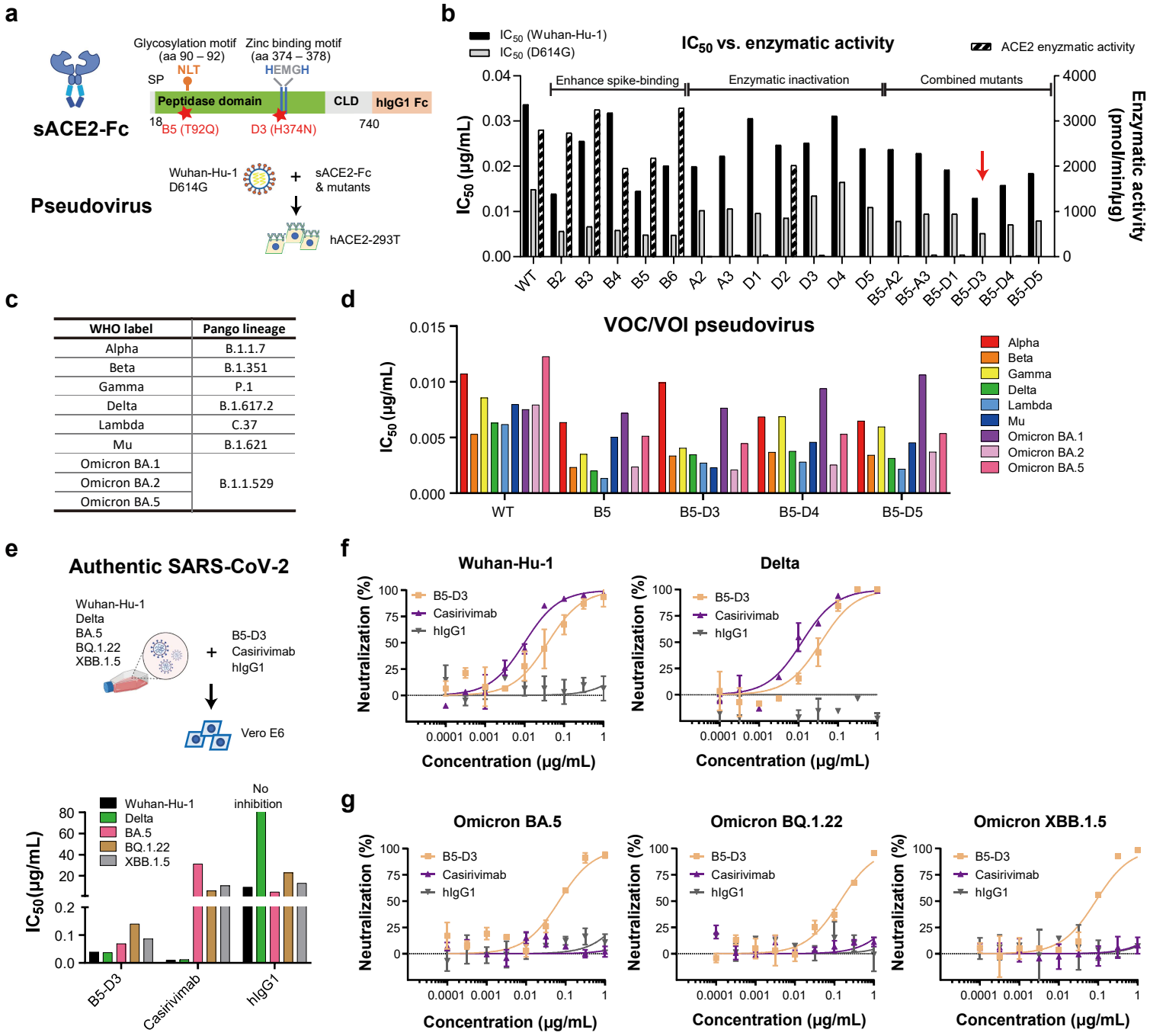
a
sACE2-Fc
Glycosylation motif (aa 90 – 92)
Zinc binding motif (aa 374 – 378)
NLT
HEMGH
SP
Peptidase domain
CLD
hIgG1 Fc
18
740
B5 (T92Q)
D3 (H374N)
Pseudovirus
Wuhan-Hu-1 D614G
sACE2-Fc & mutants
hACE2-293T
b
IC50 (Wuhan-Hu-1)
IC50 (D614G)
IC50 vs. enzymatic activity
ACE2 enyzmatic activity
Enhance spike-binding
Enzymatic inactivation
Combined mutants
IC50 (μg/mL)
Enzymatic activity (pmol/min/μg)
WT B2 B3 B4 B5 B6 A2 A3 D1 D2 D3 D4 D5 B5-A2 B5-A3 B5-D1 B5-D3 B5-D4 B5-D5
c
WHO label | Pango lineage
Alpha | B.1.1.7
Beta | B.1.351
Gamma | P.1
Delta | B.1.617.2
Lambda | C.37
Mu | B.1.621
Omicron BA.1
Omicron BA.2
Omicron BA.5
B.1.1.529
d
VOC/VOI pseudovirus
IC50 (μg/mL)
WT B5 B5-D3 B5-D4 B5-D5
Alpha
Beta
Gamma
Delta
Lambda
Mu
Omicron BA.1
Omicron BA.2
Omicron BA.5
e
Authentic SARS-CoV-2
Wuhan-Hu-1
Delta
BA.5
BQ.1.22
XBB.1.5
B5-D3
Casirivimab
hIgG1
Vero E6
IC50(μg/mL)
No inhibition
B5-D3
Casirivimab
hIgG1
f
Wuhan-Hu-1
Delta
Neutralization (%)
Concentration (μg/mL)
g
Omicron BA.5
Omicron BQ.1.22
Omicron XBB.1.5

Figure 1

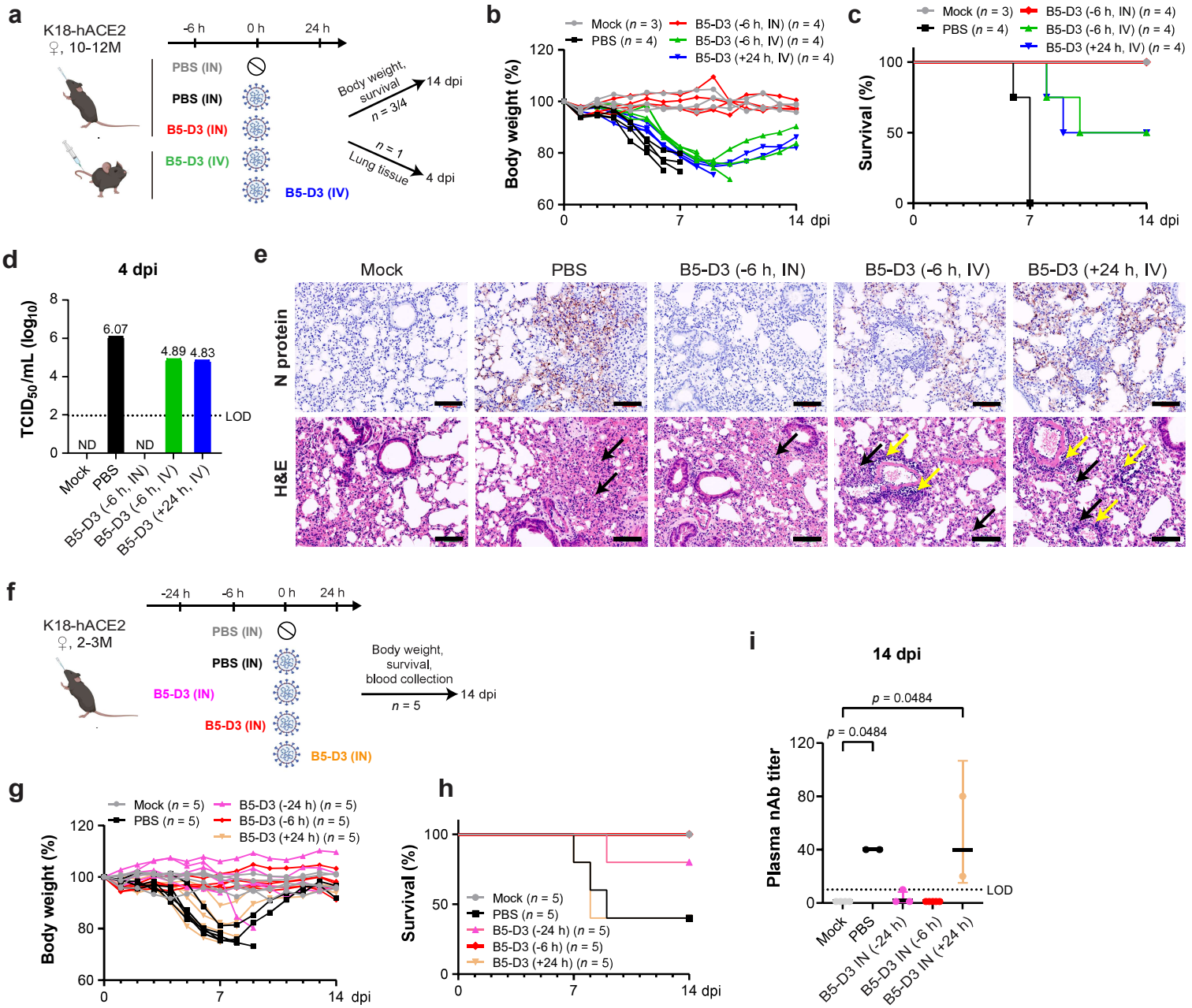
a
K18-hACE2
♀, 10-12M
-6 h
0 h
24 h
PBS (IN)
PBS (IN)
B5-D3 (IN)
B5-D3 (IV)
B5-D3 (IV)
Body weight, survival
n = 3/4
14 dpi
n = 1
Lung tissue
4 dpi
b
Mock (n = 3)
PBS (n = 4)
B5-D3 (-6 h, IN) (n = 4)
B5-D3 (-6 h, IV) (n = 4)
B5-D3 (+24 h, IV) (n = 4)
Body weight (%)
14 dpi
c
Survival (%)
14 dpi
d
4 dpi
TCID50/mL (log10)
6.07
4.89
4.83
ND
ND
LOD
Mock
PBS
B5-D3 (-6 h, IN)
B5-D3 (-6 h, IV)
B5-D3 (+24 h, IV)
e
Mock
PBS
B5-D3 (-6 h, IN)
B5-D3 (-6 h, IV)
B5-D3 (+24 h, IV)
N protein
H&E
f
K18-hACE2
♀, 2-3M
-24 h
-6 h
0 h
24 h
PBS (IN)
PBS (IN)
B5-D3 (IN)
B5-D3 (IN)
B5-D3 (IN)
Body weight, survival, blood collection
n = 5
14 dpi
g
Mock (n = 5)
PBS (n = 5)
B5-D3 (-24 h) (n = 5)
B5-D3 (-6 h) (n = 5)
B5-D3 (+24 h) (n = 5)
Body weight (%)
14 dpi
h
Survival (%)
Mock (n = 5)
PBS (n = 5)
B5-D3 (-24 h) (n = 5)
B5-D3 (-6 h) (n = 5)
B5-D3 (+24 h) (n = 5)
14 dpi
i
14 dpi
p = 0.0484
p = 0.0484
Plasma nAb titer
LOD
Mock
PBS
B5-D3 IN (-24 h)
B5-D3 IN (-6 h)
B5-D3 IN (+24 h)

Figure 2

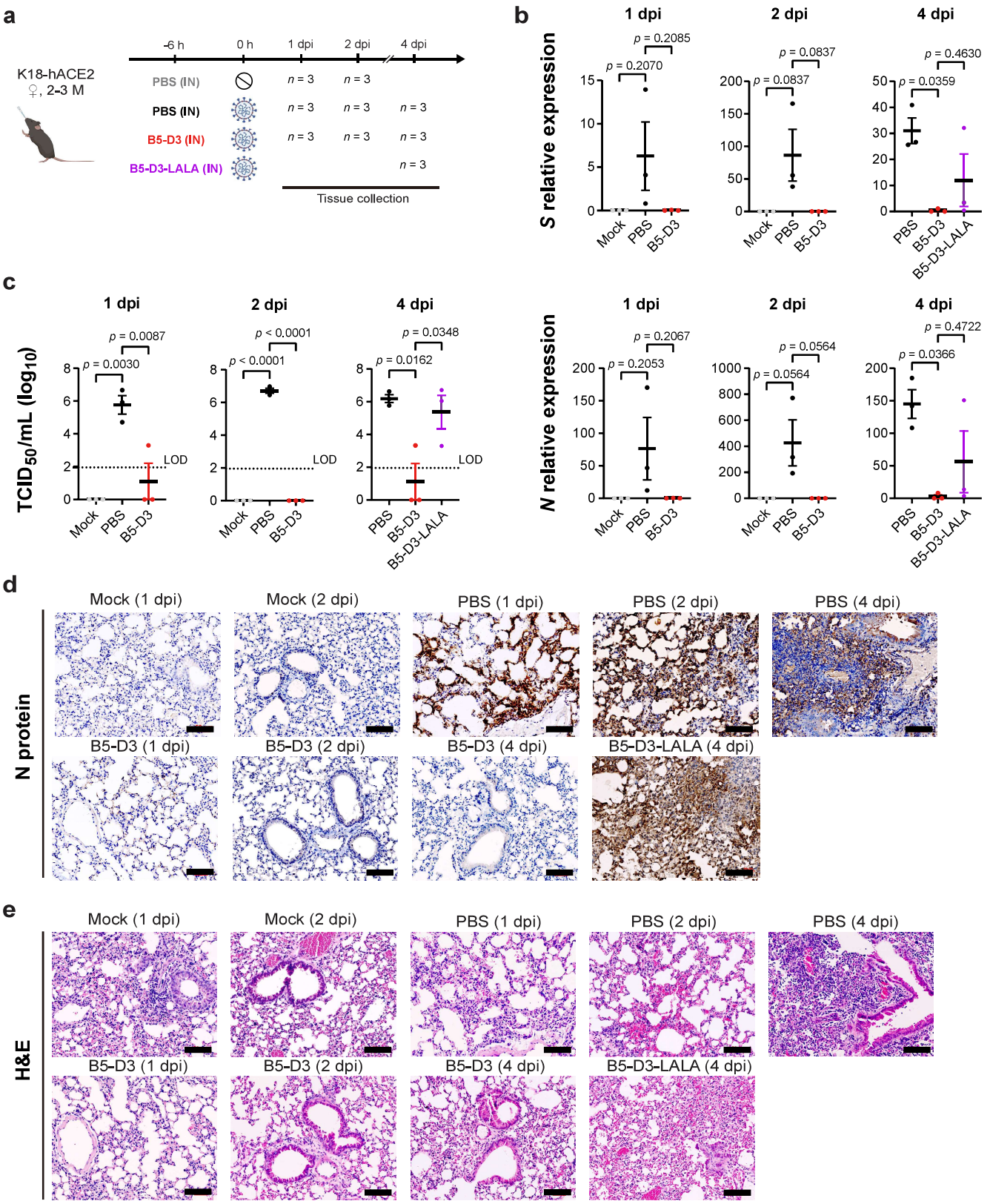
a
K18-hACE2
♀, 2-3 M
-6 h
0 h
1 dpi
2 dpi
4 dpi
PBS (IN)
n = 3
PBS (IN)
B5-D3 (IN)
B5-D3-LALA (IN)
Tissue collection
b
1 dpi
2 dpi
4 dpi
S relative expression
p = 0.2085
p = 0.2070
p = 0.0837
p = 0.0837
p = 0.4630
p = 0.0359
Mock
PBS
B5-D3
B5-D3-LALA
c
TCID50/mL (log10)
p = 0.0087
p = 0.0030
p < 0.0001
p < 0.0001
p = 0.0348
p = 0.0162
LOD
N relative expression
p = 0.2067
p = 0.2053
p = 0.0564
p = 0.0564
p = 0.4722
p = 0.0366
d
N protein
Mock (1 dpi)
Mock (2 dpi)
PBS (1 dpi)
PBS (2 dpi)
PBS (4 dpi)
B5-D3 (1 dpi)
B5-D3 (2 dpi)
B5-D3 (4 dpi)
B5-D3-LALA (4 dpi)
e
H&E
Mock (1 dpi)
Mock (2 dpi)
PBS (1 dpi)
PBS (2 dpi)
PBS (4 dpi)
B5-D3 (1 dpi)
B5-D3 (2 dpi)
B5-D3 (4 dpi)
B5-D3-LALA (4 dpi)

Figure 3

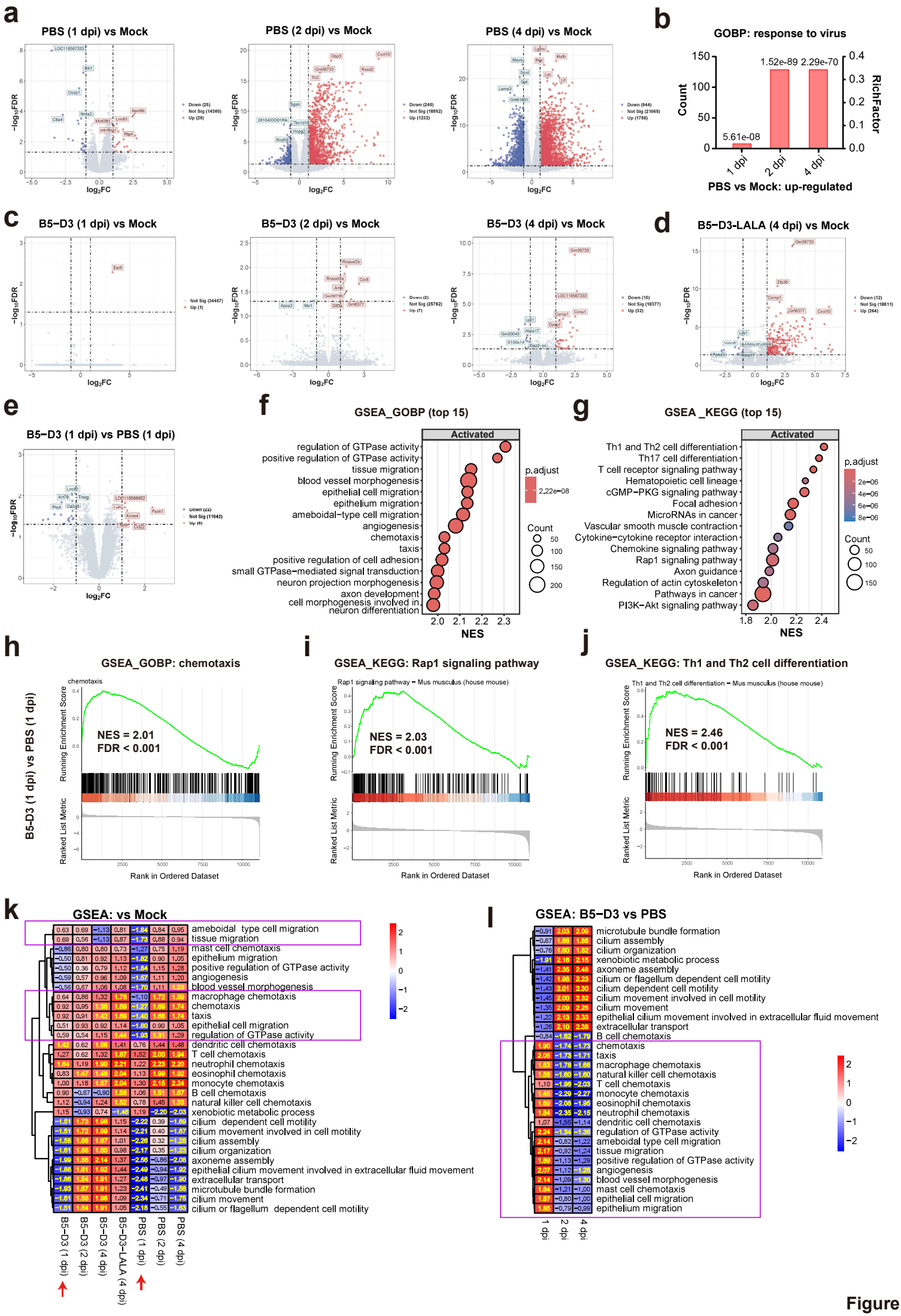
a
PBS (1 dpi) vs Mock
PBS (2 dpi) vs Mock
PBS (4 dpi) vs Mock
−log10FDR
log2FC
Down (25)
Not Sig (14360)
Up (26)
Down (240)
Not Sig (18952)
Up (1232)
Down (944)
Not Sig (21065)
Up (1756)
b
GOBP: response to virus
Count
RichFactor
5.61e-08
1.52e-89
2.29e-70
1 dpi
2 dpi
4 dpi
PBS vs Mock: up-regulated
c
B5−D3 (1 dpi) vs Mock
B5−D3 (2 dpi) vs Mock
B5−D3 (4 dpi) vs Mock
Not Sig (34457)
Up (1)
Down (2)
Not Sig (25762)
Up (7)
Down (10)
Not Sig (18377)
Up (32)
d
B5−D3-LALA (4 dpi) vs Mock
Down (12)
Not Sig (18811)
Up (264)
e
B5−D3 (1 dpi) vs PBS (1 dpi)
Down (22)
Not Sig (11042)
Up (0)
f
GSEA_GOBP (top 15)
Activated
regulation of GTPase activity
positive regulation of GTPase activity
tissue migration
blood vessel morphogenesis
epithelial cell migration
epithelium migration
ameboidal−type cell migration
angiogenesis
chemotaxis
taxis
positive regulation of cell adhesion
small GTPase−mediated signal transduction
neuron projection morphogenesis
axon development
cell morphogenesis involved in neuron differentiation
p.adjust
2.22e−08
Count
NES
g
GSEA _KEGG (top 15)
Activated
Th1 and Th2 cell differentiation
Th17 cell differentiation
T cell receptor signaling pathway
Hematopoietic cell lineage
cGMP−PKG signaling pathway
Focal adhesion
MicroRNAs in cancer
Vascular smooth muscle contraction
Cytokine−cytokine receptor interaction
Chemokine signaling pathway
Rap1 signaling pathway
Axon guidance
Regulation of actin cytoskeleton
Pathways in cancer
PI3K−Akt signaling pathway
p.adjust
Count
NES
h
GSEA_GOBP: chemotaxis
B5-D3 (1 dpi) vs PBS (1 dpi)
chemotaxis
NES = 2.01
FDR < 0.001
Running Enrichment Score
Ranked List Metric
Rank in Ordered Dataset
i
GSEA_KEGG: Rap1 signaling pathway
Rap1 signaling pathway − Mus musculus (house mouse)
NES = 2.03
FDR < 0.001
Running Enrichment Score
Ranked List Metric
Rank in Ordered Dataset
j
GSEA_KEGG: Th1 and Th2 cell differentiation
Th1 and Th2 cell differentiation − Mus musculus (house mouse)
NES = 2.46
FDR < 0.001
Running Enrichment Score
Ranked List Metric
Rank in Ordered Dataset
k
GSEA: vs Mock
ameboidal type cell migration
tissue migration
mast cell chemotaxis
epithelium migration
positive regulation of GTPase activity
angiogenesis
blood vessel morphogenesis
macrophage chemotaxis
chemotaxis
taxis
epithelial cell migration
regulation of GTPase activity
dendritic cell chemotaxis
T cell chemotaxis
neutrophil chemotaxis
eosinophil chemotaxis
monocyte chemotaxis
B cell chemotaxis
natural killer cell chemotaxis
xenobiotic metabolic process
cilium dependent cell motility
cilium movement involved in cell motility
cilium assembly
cilium organization
axoneme assembly
epithelial cilium movement involved in extracellular fluid movement
extracellular transport
microtubule bundle formation
cilium movement
cilium or flagellum dependent cell motility
B5−D3 (1 dpi)
B5−D3 (2 dpi)
B5−D3 (4 dpi)
B5−D3−LALA (4 dpi)
PBS (1 dpi)
PBS (2 dpi)
PBS (4 dpi)
l
GSEA: B5−D3 vs PBS
microtubule bundle formation
cilium assembly
cilium organization
xenobiotic metabolic process
axoneme assembly
cilium or flagellum dependent cell motility
cilium dependent cell motility
cilium movement involved in cell motility
cilium movement
epithelial cilium movement involved in extracellular fluid movement
extracellular transport
B cell chemotaxis
chemotaxis
taxis
macrophage chemotaxis
natural killer cell chemotaxis
T cell chemotaxis
monocyte chemotaxis
eosinophil chemotaxis
neutrophil chemotaxis
dendritic cell chemotaxis
regulation of GTPase activity
ameboidal type cell migration
tissue migration
positive regulation of GTPase activity
angiogenesis
blood vessel morphogenesis
mast cell chemotaxis
epithelial cell migration
epithelium migration
1 dpi
2 dpi
4 dpi

Figure 4

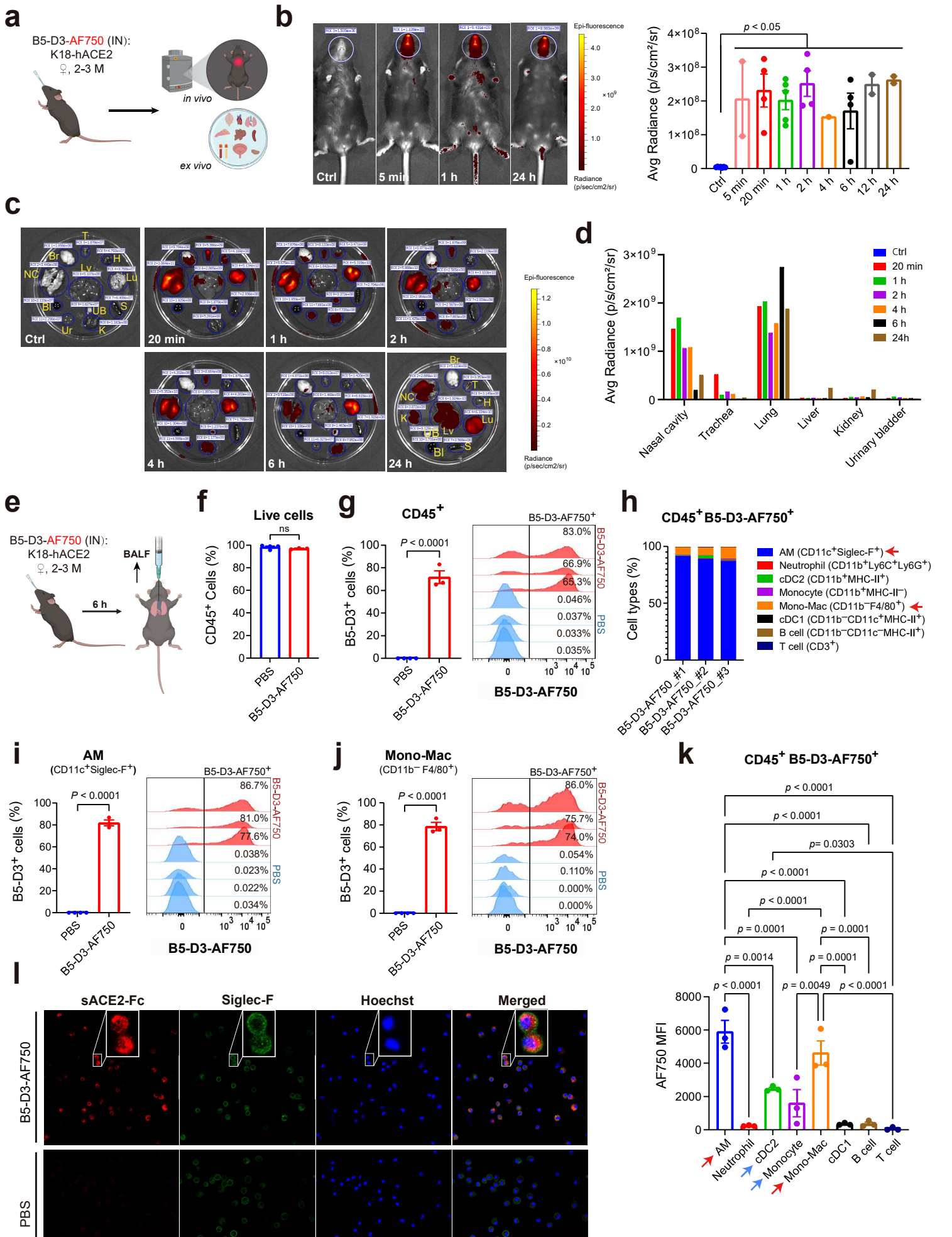
a
B5-D3-AF750 (IN):
K18-hACE2
♀, 2-3 M
in vivo
ex vivo
b
Ctrl
5 min
1 h
24 h
Epi-fluorescence
Radiance (p/sec/cm2/sr)
Avg Radiance (p/s/cm²/sr)
p < 0.05
Ctrl
5 min
20 min
1 h
2 h
4 h
6 h
12 h
24 h
c
Ctrl
20 min
1 h
2 h
4 h
6 h
24 h
Epi-fluorescence
Radiance (p/sec/cm2/sr)
d
Avg Radiance (p/s/cm²/sr)
Ctrl
20 min
1 h
2 h
4 h
6 h
24h
Nasal cavity
Trachea
Lung
Liver
Kidney
Urinary bladder
e
B5-D3-AF750 (IN):
K18-hACE2
♀, 2-3 M
6 h
BALF
f
Live cells
ns
CD45⁺ Cells (%)
PBS
B5-D3-AF750
g
CD45⁺
P < 0.0001
B5-D3⁺ cells (%)
B5-D3-AF750⁺
83.0%
66.9%
65.3%
0.046%
0.037%
0.033%
0.035%
B5-D3-AF750
PBS
B5-D3-AF750
h
CD45⁺B5-D3-AF750⁺
Cell types (%)
AM (CD11c⁺Siglec-F⁺)
Neutrophil (CD11b⁺Ly6C⁺Ly6G⁺)
cDC2 (CD11b⁺MHC-II⁺)
Monocyte (CD11b⁺MHC-II⁻)
Mono-Mac (CD11b⁻F4/80⁺)
cDC1 (CD11b⁻CD11c⁺MHC-II⁺)
B cell (CD11b⁻CD11c⁻MHC-II⁺)
T cell (CD3⁺)
B5-D3-AF750_#1
B5-D3-AF750_#2
B5-D3-AF750_#3
i
AM
(CD11c⁺Siglec-F⁺)
P < 0.0001
B5-D3⁺ cells (%)
B5-D3-AF750⁺
86.7%
81.0%
77.6%
0.038%
0.023%
0.022%
0.034%
B5-D3-AF750
PBS
j
Mono-Mac
(CD11b⁻ F4/80⁺)
P < 0.0001
B5-D3⁺ cells (%)
B5-D3-AF750⁺
86.0%
75.7%
74.0%
0.054%
0.110%
0.000%
0.000%
B5-D3-AF750
PBS
k
CD45⁺ B5-D3-AF750⁺
p < 0.0001
p < 0.0001
p= 0.0303
p < 0.0001
p < 0.0001
p = 0.0001
p = 0.0001
p = 0.0014
p = 0.0001
p < 0.0001
p = 0.0049
p < 0.0001
AF750 MFI
AM
Neutrophil
cDC2
Monocyte
Mono-Mac
cDC1
B cell
T cell
l
sACE2-Fc
Siglec-F
Hoechst
Merged
B5-D3-AF750
PBS

Figure 5

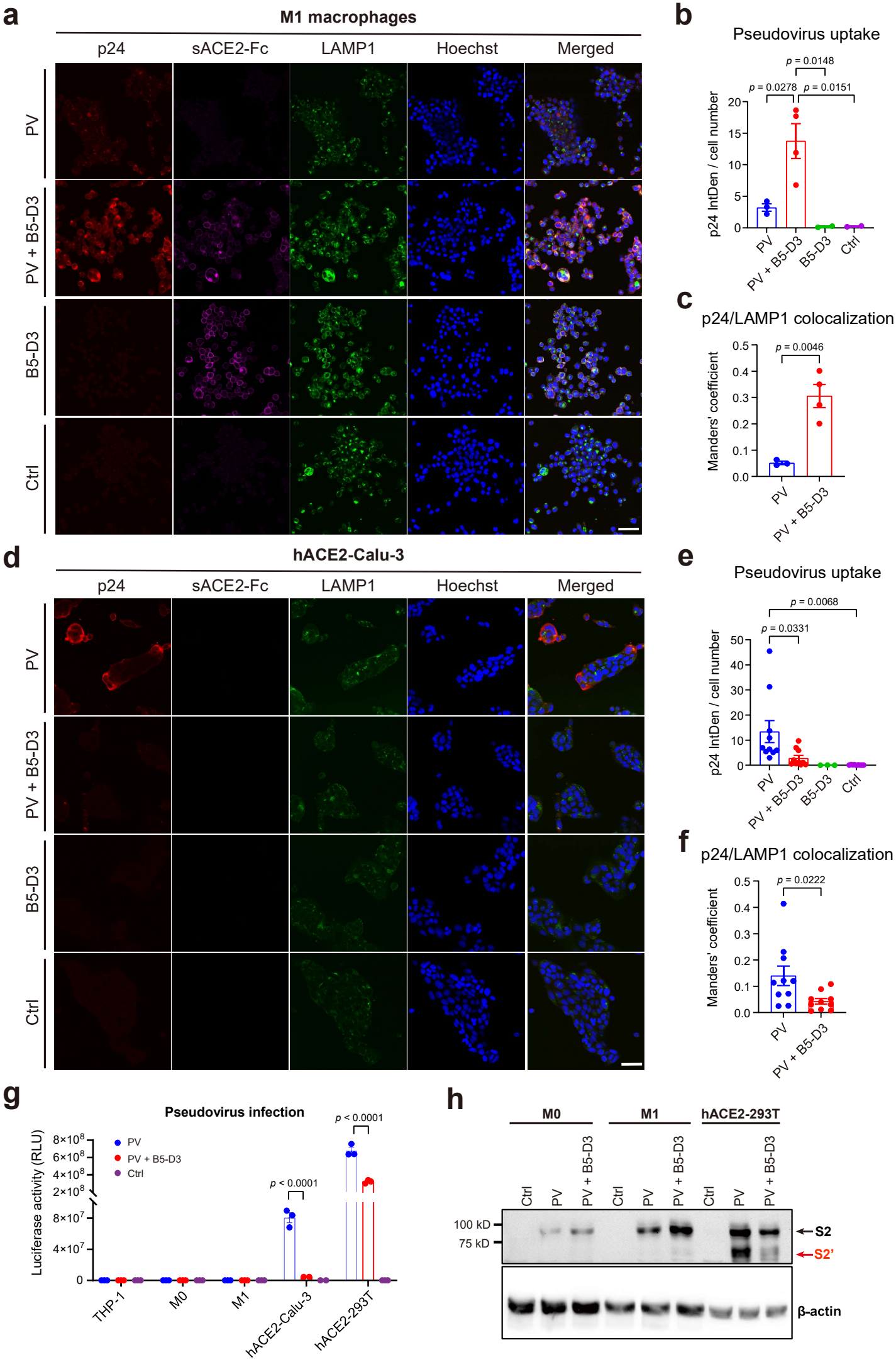
a
M1 macrophages
p24
sACE2-Fc
LAMP1
Hoechst
Merged
PV
PV + B5-D3
B5-D3
Ctrl
b
Pseudovirus uptake
p = 0.0148
p = 0.0278
p = 0.0151
p24 IntDen / cell number
PV
PV + B5-D3
B5-D3
Ctrl
c
p24/LAMP1 colocalization
p = 0.0046
Manders' coefficient
PV
PV + B5-D3
d
hACE2-Calu-3
p24
sACE2-Fc
LAMP1
Hoechst
Merged
PV
PV + B5-D3
B5-D3
Ctrl
e
Pseudovirus uptake
p = 0.0068
p = 0.0331
p24 IntDen / cell number
PV
PV + B5-D3
B5-D3
Ctrl
f
p24/LAMP1 colocalization
p = 0.0222
Manders' coefficient
PV
PV + B5-D3
g
Pseudovirus infection
PV
PV + B5-D3
Ctrl
p < 0.0001
p < 0.0001
Luciferase activity (RLU)
THP-1
M0
M1
hACE2-Calu-3
hACE2-293T
h
M0
M1
hACE2-293T
Ctrl
PV
PV + B5-D3
100 kD
75 kD
S2
S2'
β-actin

Figure 6

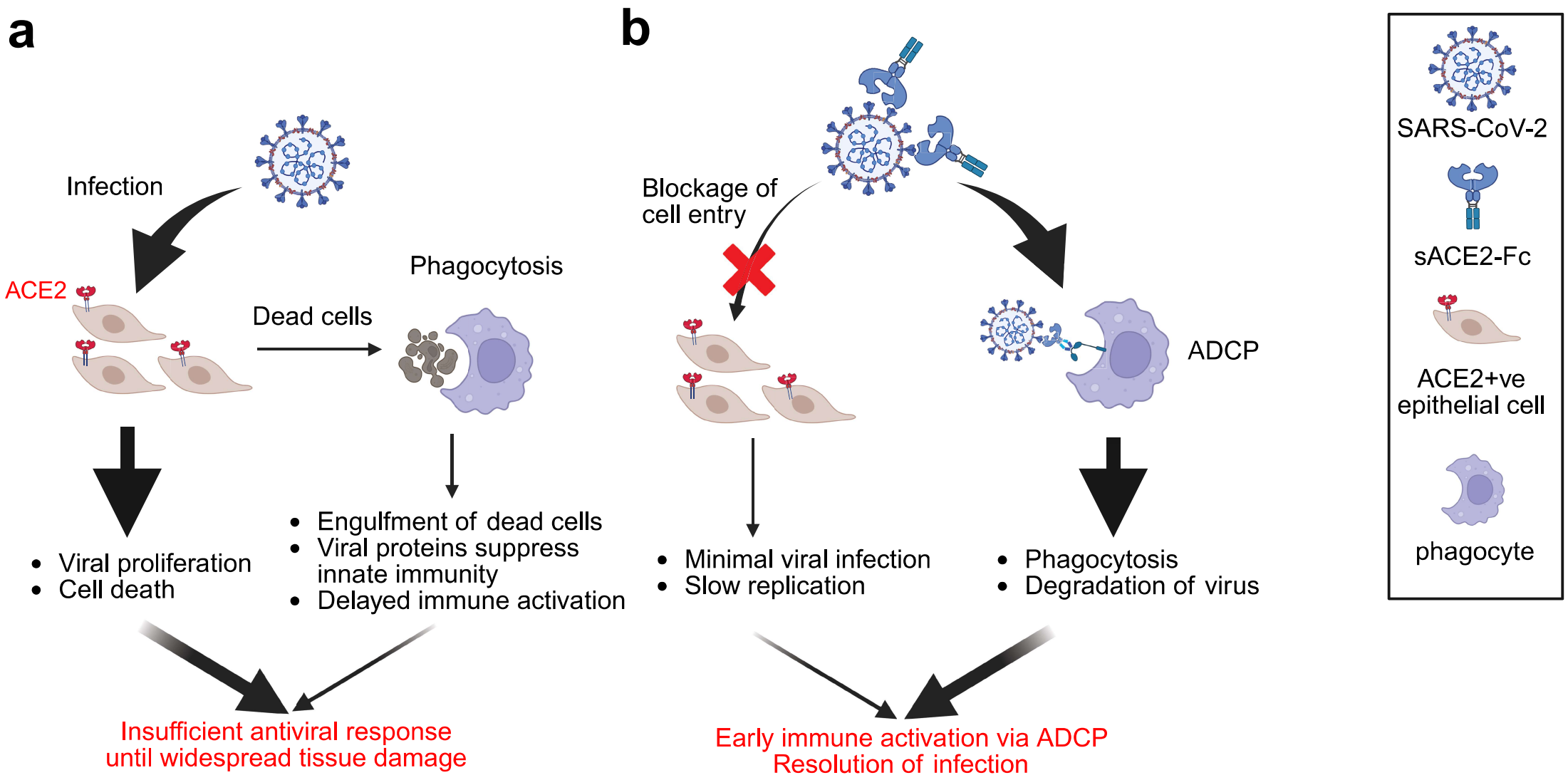
a
Infection
ACE2
Dead cells
Phagocytosis
Viral proliferation
Cell death
Engulfment of dead cells
Viral proteins suppress innate immunity
Delayed immune activation
Insufficient antiviral response until widespread tissue damage
b
Blockage of cell entry
ADCP
Minimal viral infection
Slow replication
Phagocytosis
Degradation of virus
Early immune activation via ADCP
Resolution of infection
SARS-CoV-2
sACE2-Fc
ACE2+ve epithelial cell
phagocyte

Figure 7

Supplementary Information for

Redirection of SARS-CoV-2 to Phagocytes by Intranasal sACE2-Fc as a Universal Decoy Confers Complete Prophylactic Protection

Jingyi Wang *et al.*

Corresponding authors: Leo L. Poon, llmpoon@hku.hk; Bo Feng, fengbo@cuhk.edu.hk

This PDF file includes:

Supplementary Fig. 1 to 18

Supplementary Tables 1 and 2

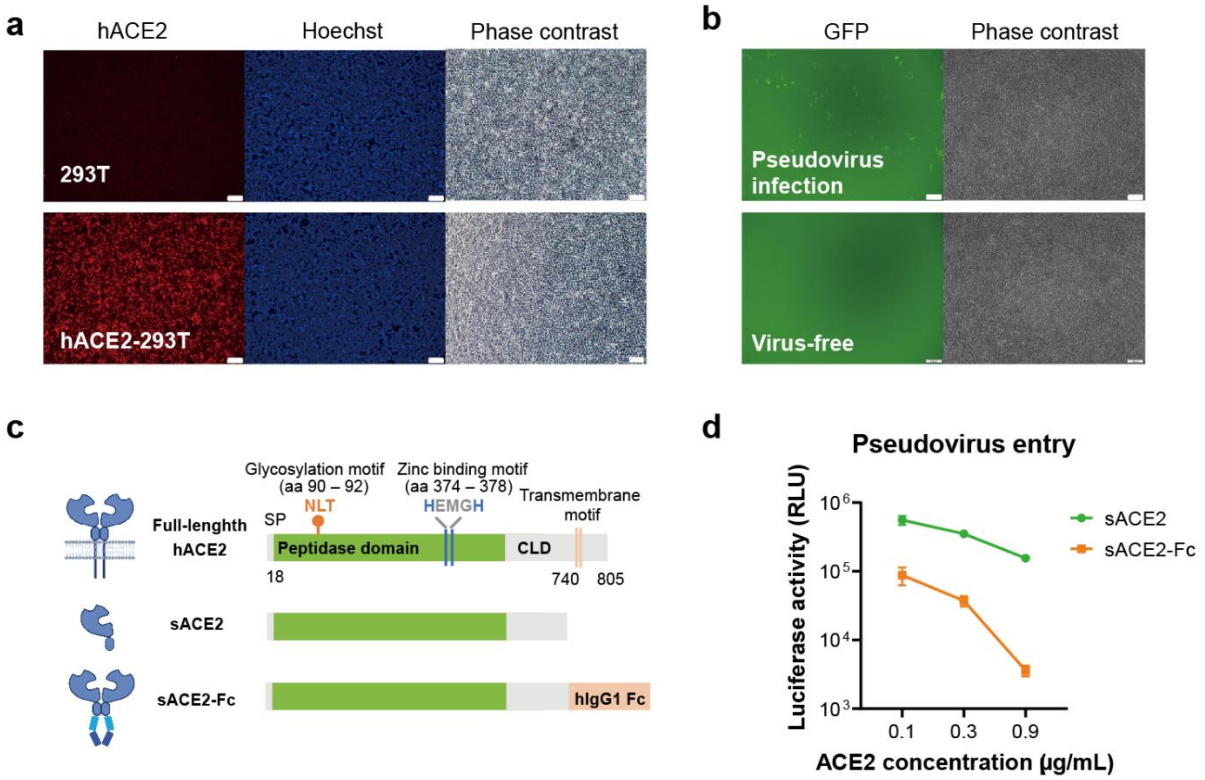

Supplementary Fig. 1 Establishment of the pseudoviral infection platform and generation of sACE2 decoys. a Microscopic images show the expression of full length human ACE2 (hACE2) in stable hACE2-293T cells established by lentiviral transduction (Scale bar = 100 μm). Immunostaining was performed using antibody specific to hACE2 (Abcam # ab15348). **b** Representative fluorescence and phase contrast images showing GFP expression in hACE2-293T cells with and without infection by pseudovirus carrying the Wuhan-Hu-1 spike protein (Scale bar = 100 μm). **c** Schematic diagrams of hACE2 (top), sACE2 (middle), and sACE2-Fc (bottom) molecules indicating important amino acid positions (90-92 and 374-378) for glycosylation and zinc binding. aa, amino acid. **d** Line chart comparing the neutralization efficiencies of sACE2 (green) and sACE2-Fc (orange) against Wuhan-Hu-1 pseudovirus expressing luciferase, measured in relative luminescence units (RLU). Data are presented as mean ± SD from duplicate experiments.

a

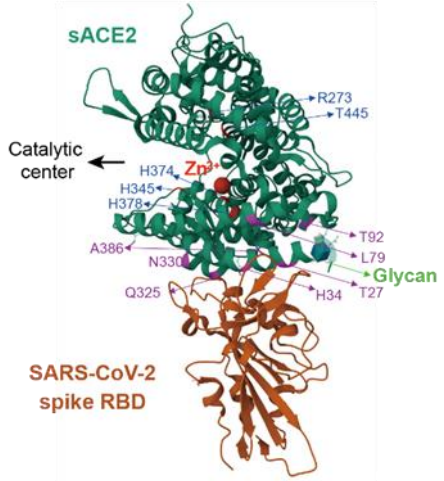

b

Type	Mutant	Mutation(s)	Alias
Spike-binding enhancement	B2	T27Y/L79T	/
	B3	T27Y/L79T/N330Y	sACE2.v2.4
	B4	H34A/T92Q/Q325P/A386L	sACE2.v1
	B5	T92Q	/
	B6	T27Y/L79T/N330Y/A386L	sACE2.v2
Enzymatic inactivation	A2	H374N/H378N	HH/NN
	A3	R273G/T445G	/
	D1	R273G	/
	D2	T445G	/
	D3	H374N	/
	D4	H378N	/
	D5	H345L	/
B5-derived	B5-A2	T92Q /H374N/H378N	/
	B5-A3	T92Q /R273G/T445G	/
	B5-D1	T92Q /R273G	/
	B5-D3	T92Q /H374N	/
	B5-D4	T92Q /H378N	/
	B5-D5	T92Q /H345L	/

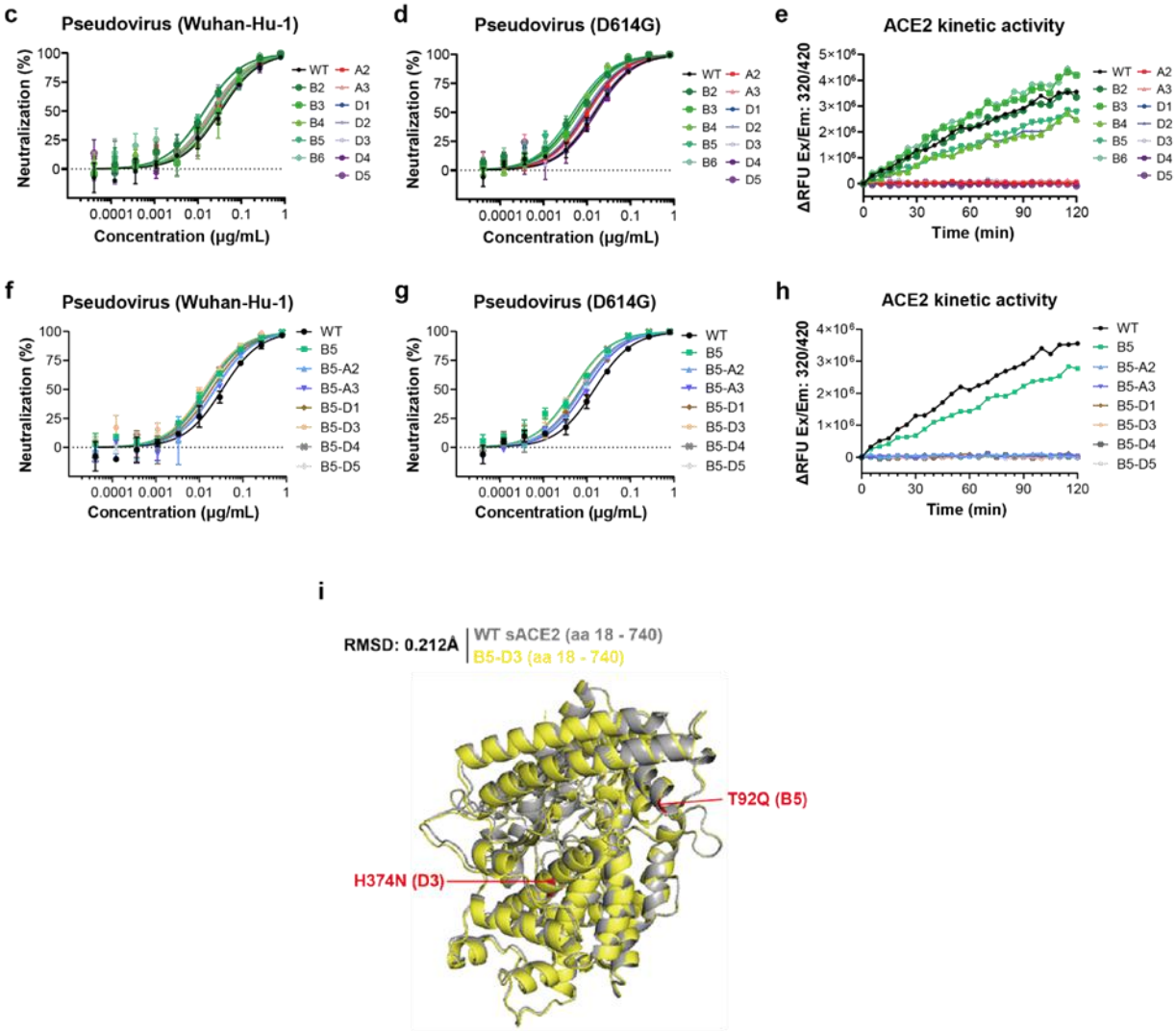

Supplementary Fig. 2 Engineering and characterization of enhanced sACE2 decoys. a 3D structural model of ACE2 (green) complexed with the SARS-CoV-2 spike receptor-binding domain (RBD, brown), highlighting mutations for spike-binding enhancement (magenta) and enzymatic inactivation (blue). Structures were adapted from Protein Data Bank (PDB ID: 6M0J). **b** List of mutations in sACE2 sequences tested for enhanced binding or enzymatic inactivation. **c**, **d** Neutralization assay results for WT sACE2-Fc and mutants (B2 to B6, A2, A3, and D1 to

D5) against Wuhan-Hu-1 (**c**) and D614G (**d**) pseudoviruses. **e** Kinetic curves showing the ACE2 enzymatic activities of WT sACE2-Fc and B2 to B6, A2, A3, D1 to D5 mutants. **f**, **g** Neutralization results for WT sACE2-Fc and mutants (B5, B5-A2, B5-A3, B5-D1, B5-D3, B5-D4 and B5-D5) against Wuhan-Hu-1 (**f**) and D614G (**g**) pseudoviruses. **h** Kinetic curves showing the ACE2 enzymatic activities of WT sACE2-Fc and B5, B5-A2, B5-A3, B5-D1, B5-D3, B5-D4 and B5-D5 mutants. **i** Conformational comparison between WT and B5-D3 sACE2. The 3D structures of WT and B5-D3 sACE2 (aa 18–740) were predicted using AlphaFold 3 and superimposed for direct comparison. The WT sACE2 structure is coloured in grey, while the B5-D3 variant is highlighted in yellow. Mutations in the B5-D3 structure are specifically marked in red. Data are presented as mean ± SD from duplicate experiments.

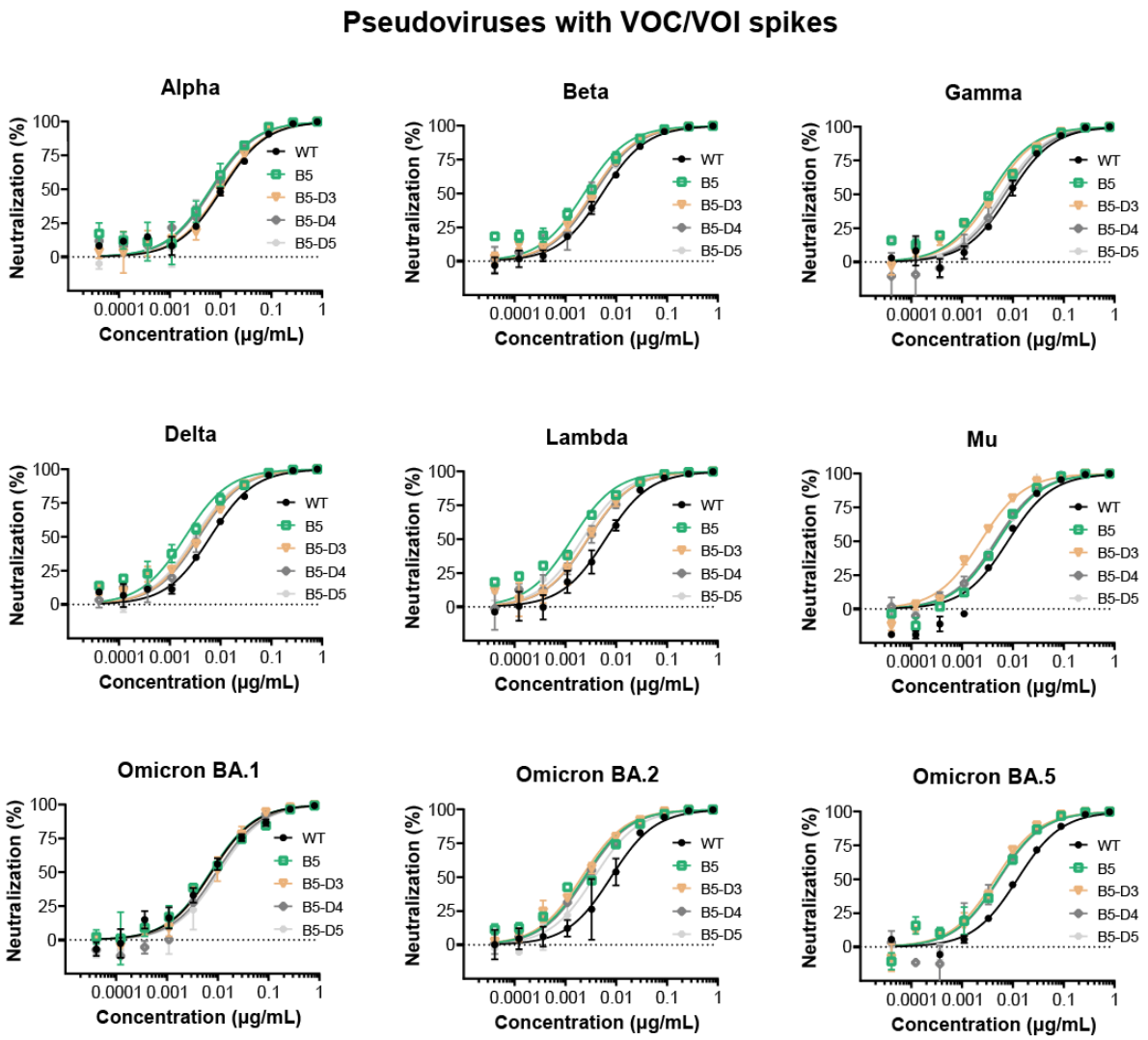

Supplementary Fig. 3 Broad-spectrum neutralization against pseudoviruses of SARS-CoV-2 VOC/VOI strains by sACE2-Fc candidate mutants. Graphical representation of dose-response curves in neutralization assays against pseudoviruses bearing spikes from various SARS-CoV-2 VOCs and VOIs. Data are presented as mean ± SD from duplicate experiments.

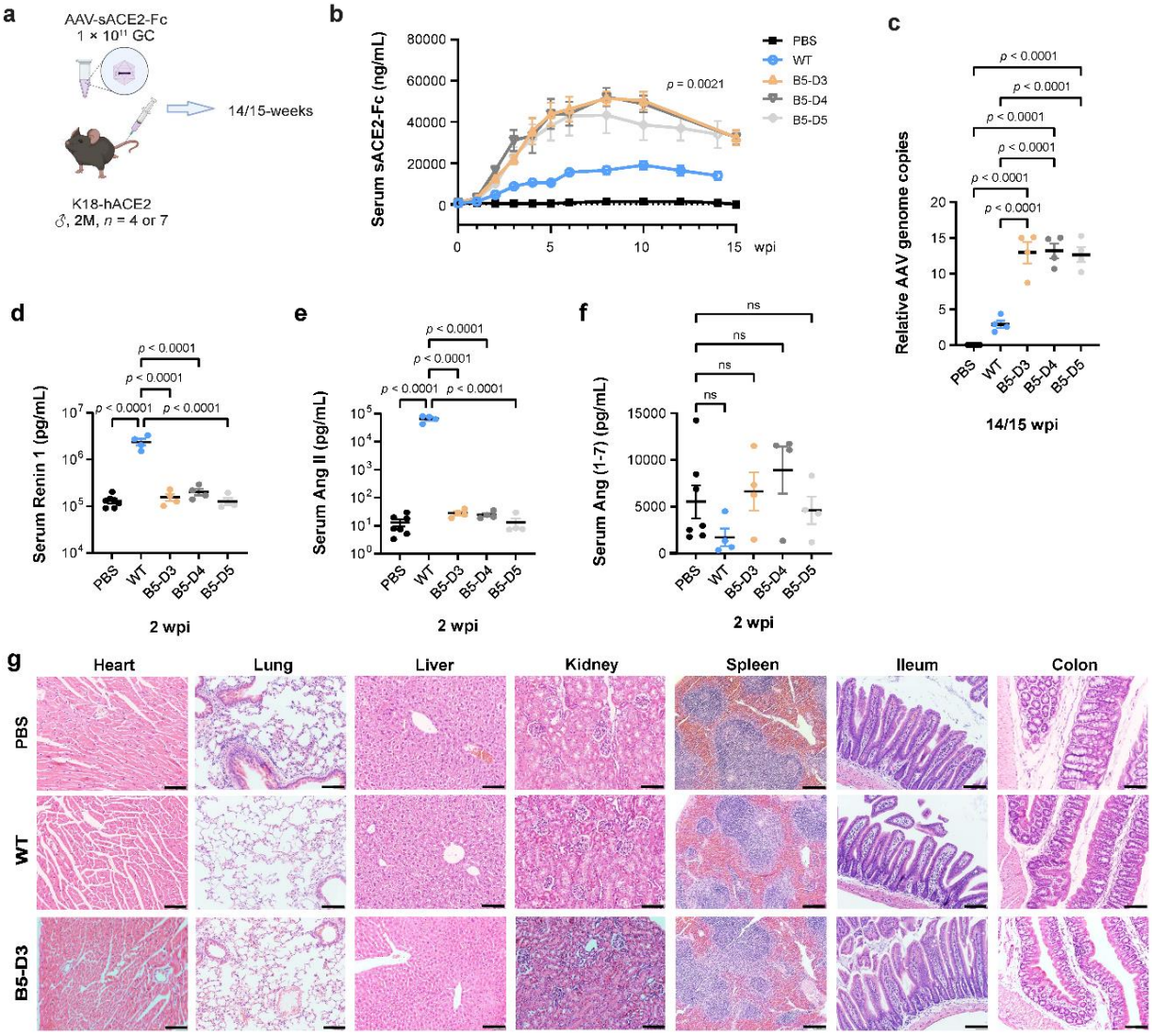

Supplementary Fig. 4 AAV-delivered prolonged overexpression of WT sACE2-Fc and candidate mutants in K18-hACE2 mice. a Schematic of AAV administration. Male K18-hACE2 mice aged 2 months received tail vein injections of either PBS (black; n = 7) or AAV carrying WT sACE2-Fc (blue), B5-D3 (orange), B5-D4 (dark grey), or B5-D5 (light grey) (n = 4 each) at a dose of 1×10^{11} GC. Mice were observed for up to 15 weeks and then sacrificed for tissue analysis. wpi, weeks post-injection; M, month. **b** Serum concentrations of sACE2-Fc were quantified via ELISA using antibodies specific to hIgG1. **c** Quantification of AAV genomes in the mouse livers at the observation endpoint. Results shown are from qPCR of genome DNA normalized to mouse *Gapdh.* **d**–**f** Concentrations of renin (**d**), Ang II (**e**), and Ang (1-7) (**f**) in sera at 2 wpi, measured via metabolite-specific ELISA. ns, not significant with p value (p) ≥ 0.05. **g** Representative H&E staining of heart, lung, liver, kidney, spleen, ileum, and colon tissues from mice in the PBS, WT sACE2-Fc, and B5-D3 treatment groups (scale bar = 50 μm). Data are presented as mean ± SEM. Statistical analyses were performed using one-way analysis of variance (ANOVA) and Tukey's multiple comparisons test following ANOVA.

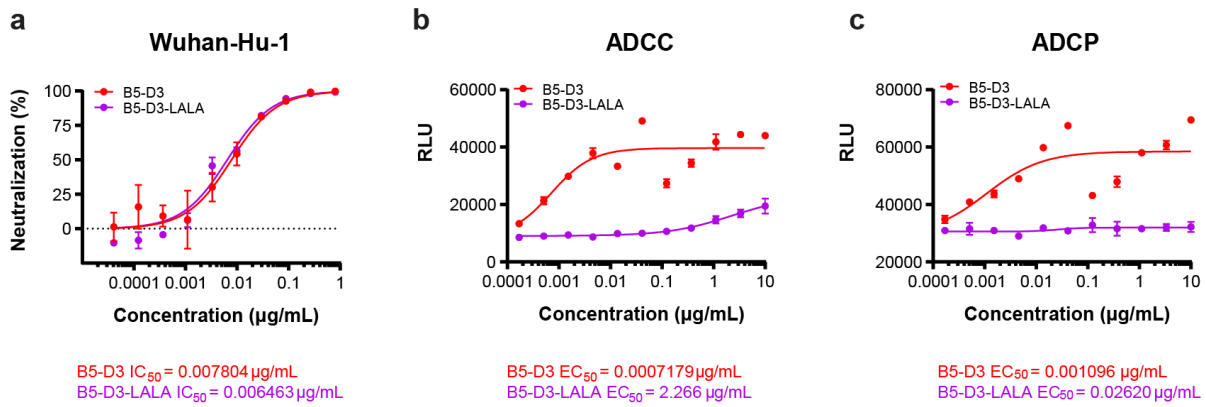

Supplementary Fig. 5 Comparison between B5-D3 and B5-D3-LALA in *in vitro* neutralization against the SARS-CoV2 pseudovirus and Fc-mediated effector functions. a Neutralization capability of B5-D3-LALA was compared to B5-D3 using an *in vitro* pseudovirus neutralization assay. IC_{50} values are indicated for each version. **b**, **c** Fc-mediated effector functions of B5-D3 and B5-D3-LALA were assessed using luciferase-based reporter cell lines. Dose-response curves and half maximal effective concentration (EC_{50}) values for antibody-dependent cellular cytotoxicity (ADCC) (**b**) and antibody-dependent cellular phagocytosis (ADCP) (**c**) are displayed. Data are presented as mean ± SD from duplicate experiments.

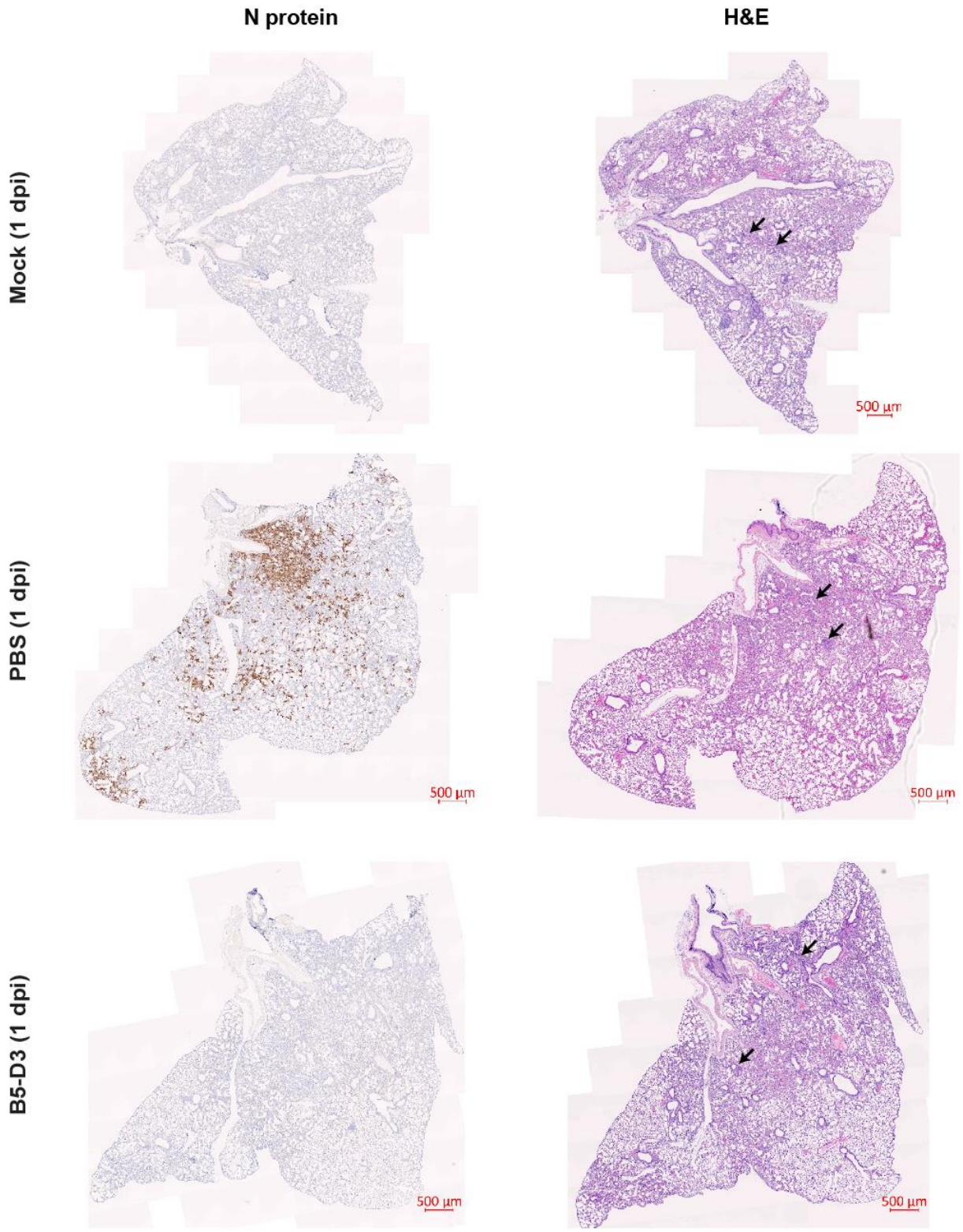

Supplementary Fig. 6 Entire sections for histological examination at 1 dpi. Fixed lung tissues were sectioned and stained for histological examination. IHC staining for viral N protein (left panels, SinoBiological # 40143-T62) and H&E staining for tissue damage (right panels) are displayed. Black arrows in H&E photos indicate areas of alveolar thickening. Scale bar = 500 µm.

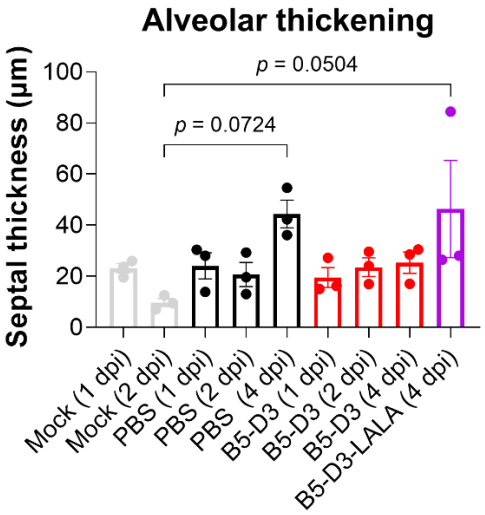

Supplementary Fig. 7 Thickening of alveolar septum in K18-hACE2 mice after SARS-CoV-2 challenge. Lung septum thickness of K18-hACE2 mice in Fig. 3 was measured from H&E staining. Data are presented as mean ± SEM, and statistical significance was determined by Tukey's multiple comparisons test.

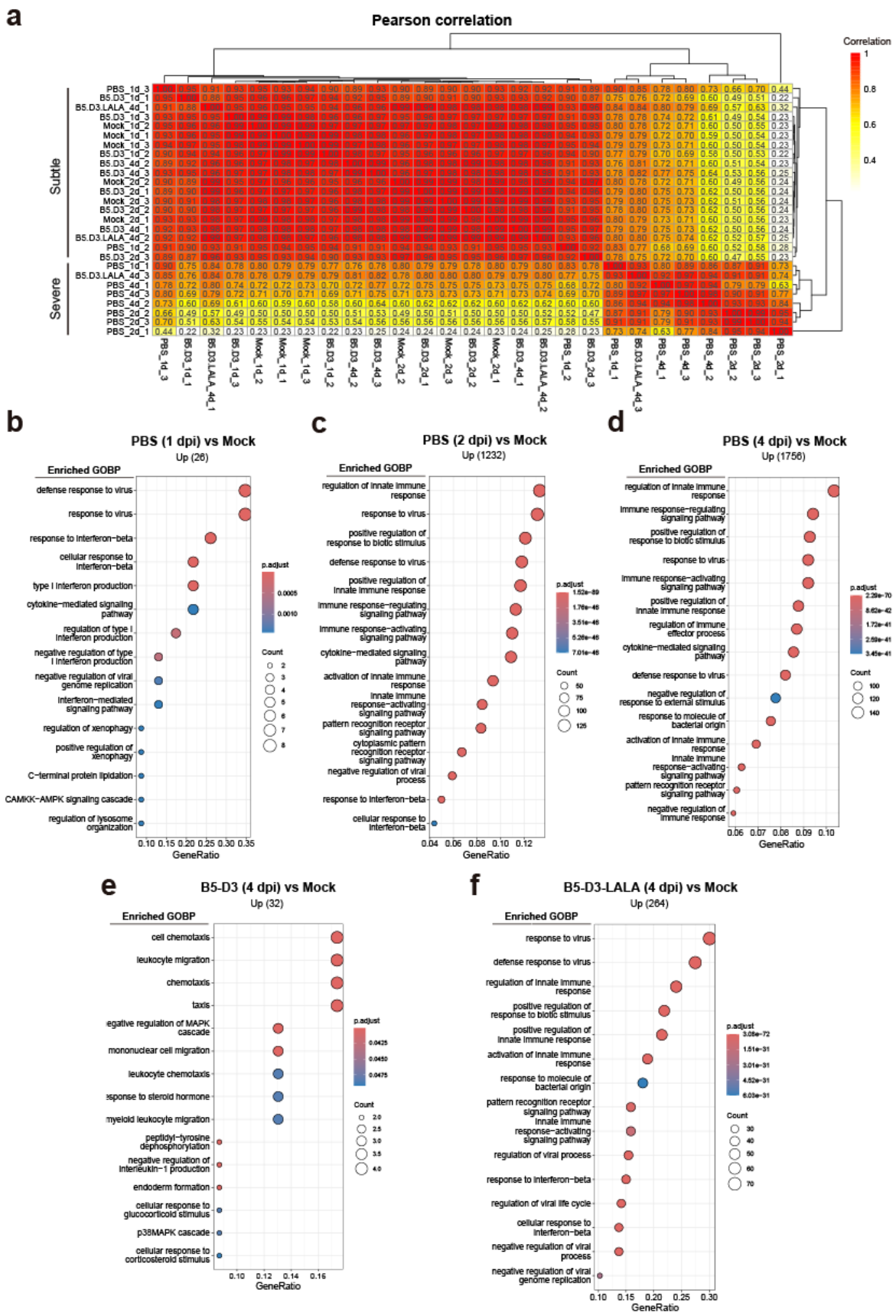

Supplementary Fig. 8 RNA-Seq analysis of K18-hACE2 mouse lungs with different pretreatments upon SARS-CoV-2 challenge. a Bulk RNA-seq was conducted on lung homogenates from K18-hACE2 mice under mock treatment ($n = 6$) or post-viral challenge at 1, 2 and 4 dpi with each time point ($n = 3$). Pearson correlation analysis was executed on 27 samples

using counts per million (CPM) data, with each cell displaying the Pearson correlation coefficient color-coded for visual ease. **b**–**f** GOBP enrichment analysis identifies biological processes enriched in up-regulated genes from comparisons at 1 (**b**), 2 (**c**), and 4 dpi (**d**) for PBS, 4 dpi for B5-D3 (**e**), and 4 dpi for B5-D3-LALA (**f**) versus the mock control, with top 15 significant terms displayed. *p*.adjust, adjusted *p* value; CAMKK, calmodulin-dependent protein kinase; AMPK, 5' adenosine monophosphate-activated protein kinase. Benjamin–Hochberg method was used for FDR adjustment.

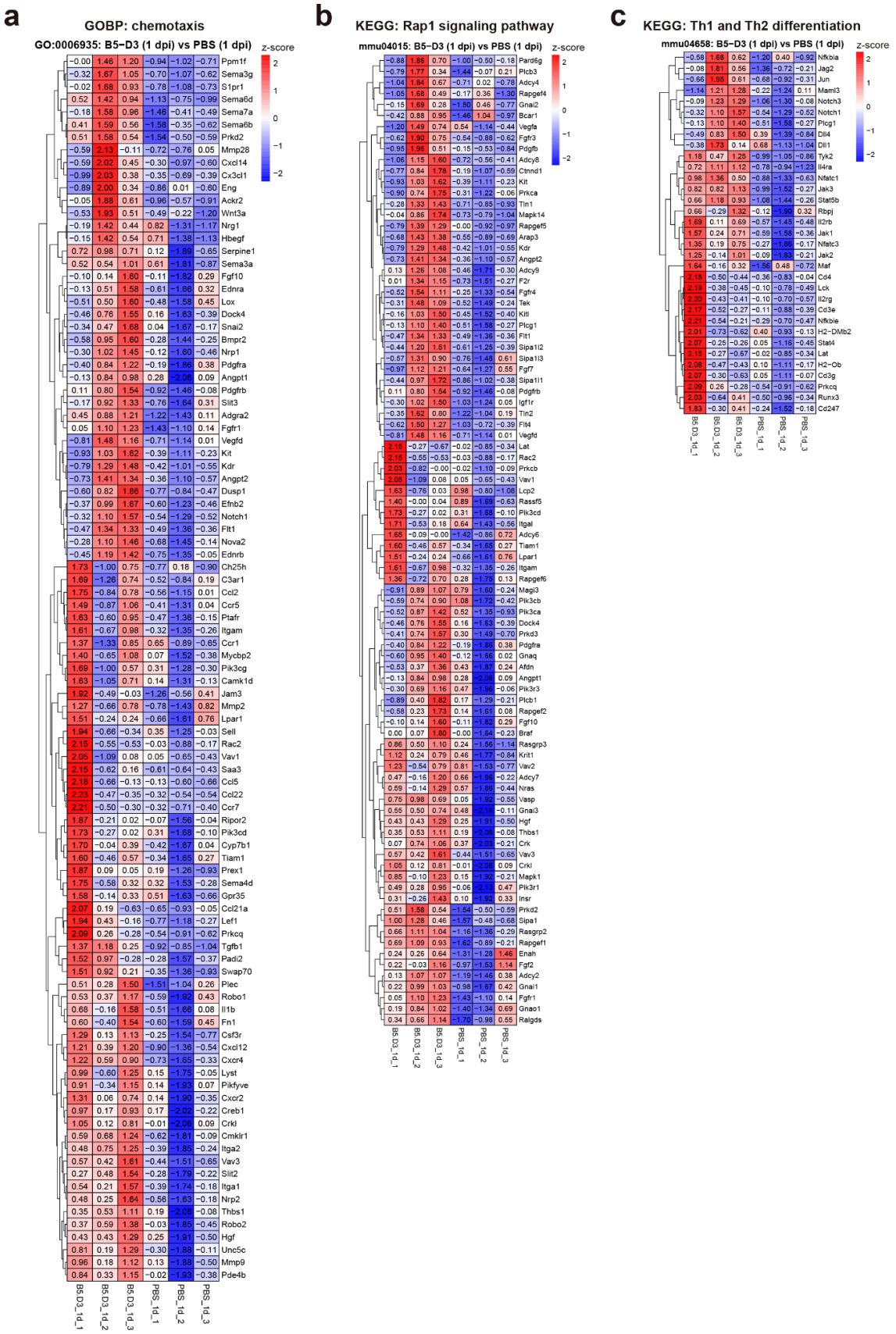

Supplementary Fig. 9 Leading-edge subsets in GSEA. a–c Z-score plots show the relative level of gene expression in the leading edge subsets from GSEA comparing B5-D3 vs PBS at 1

dpi, corresponding to chemotaxis (**a**), Rap1 signaling pathway (**b**), and Th1 and Th2 differentiation (**c**).

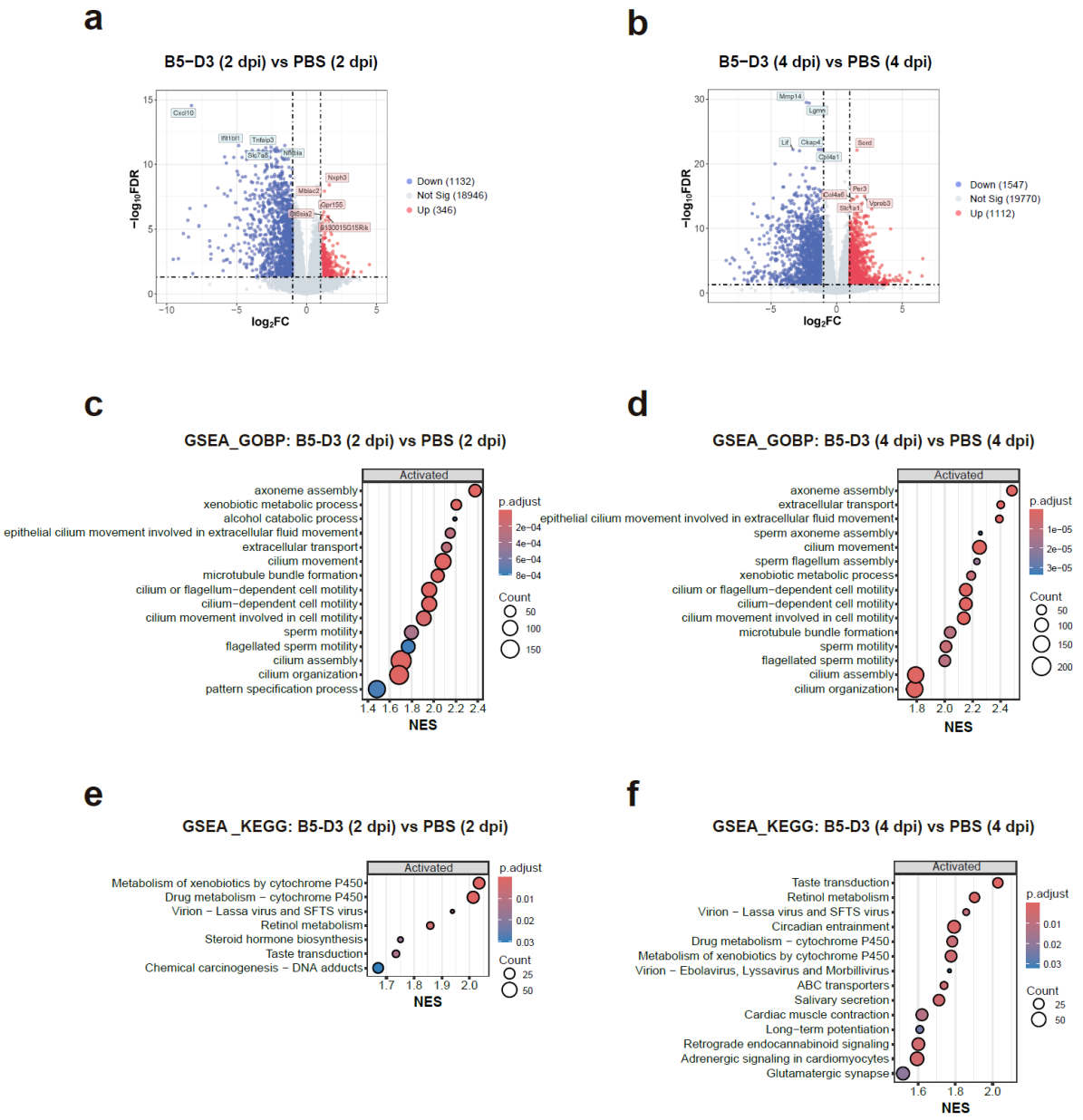

Supplementary Fig. 10 Transcriptomic comparisons between B5-D3 and PBS pretreatments in K18-hACE2 mice upon SARS-CoV-2 challenge. a, b DGE analysis between B5-D3 and PBS groups at 2 (**a**), and 4 dpi (**b**) showing up-regulated and down-regulated genes visualized in volcano plots. **c**, **d** GSEA of GOBPs significantly activated in B5-D3 groups compared to PBS groups at 2 dpi (**c**) and 4 dpi (**d**), with top 15 most significant terms displayed. **e, f** GSEA of KEGG pathways significantly activated in B5-D3 groups compared to PBS groups at 2 dpi (**e**) and 4 dpi (**f**), with all significant terms (**e**) and top 15 most significant terms (**f**) displayed. SFTS, Severe Fever with Thrombocytopenia Syndrome. Benjamin–Hochberg method was used for FDR adjustment.

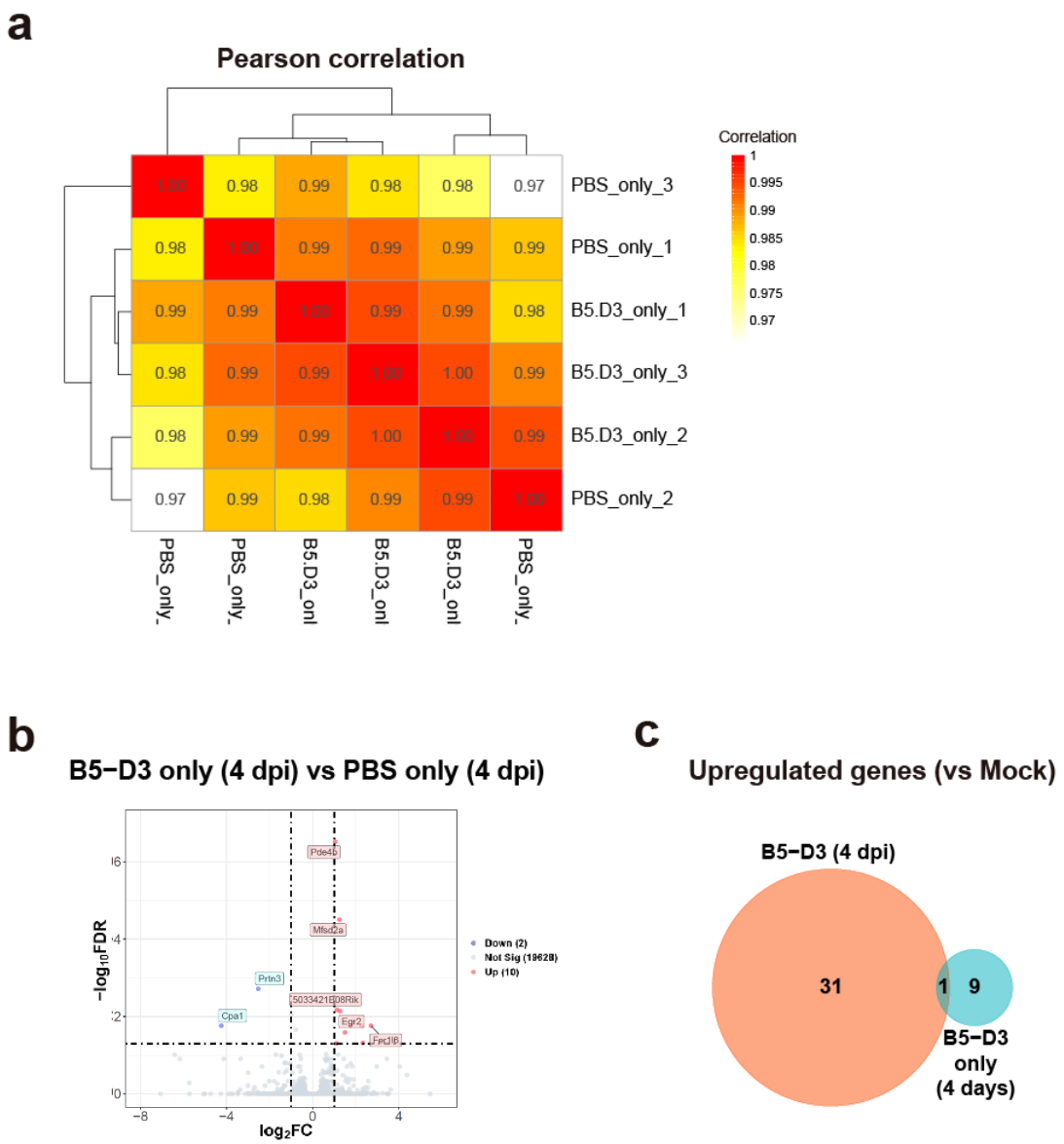

Supplementary Fig. 11 Minimal transcriptomic alterations in lungs after IN B5-D3 administration without viral challenge. a Pearson correlation analysis for lung tissues collected 4 days post-administration of IN B5-D3 or PBS in female K18-hACE2 mice (n = 3), depicting correlation coefficients. **b** Volcano plot showing differentially expressed genes between the B5-D3 treated and control groups, with significant changes marked. **c** Venn diagram showing overlaps among the upregulated genes in **b** and in B5-D3 (4 dpi) in Fig. 4**c**.

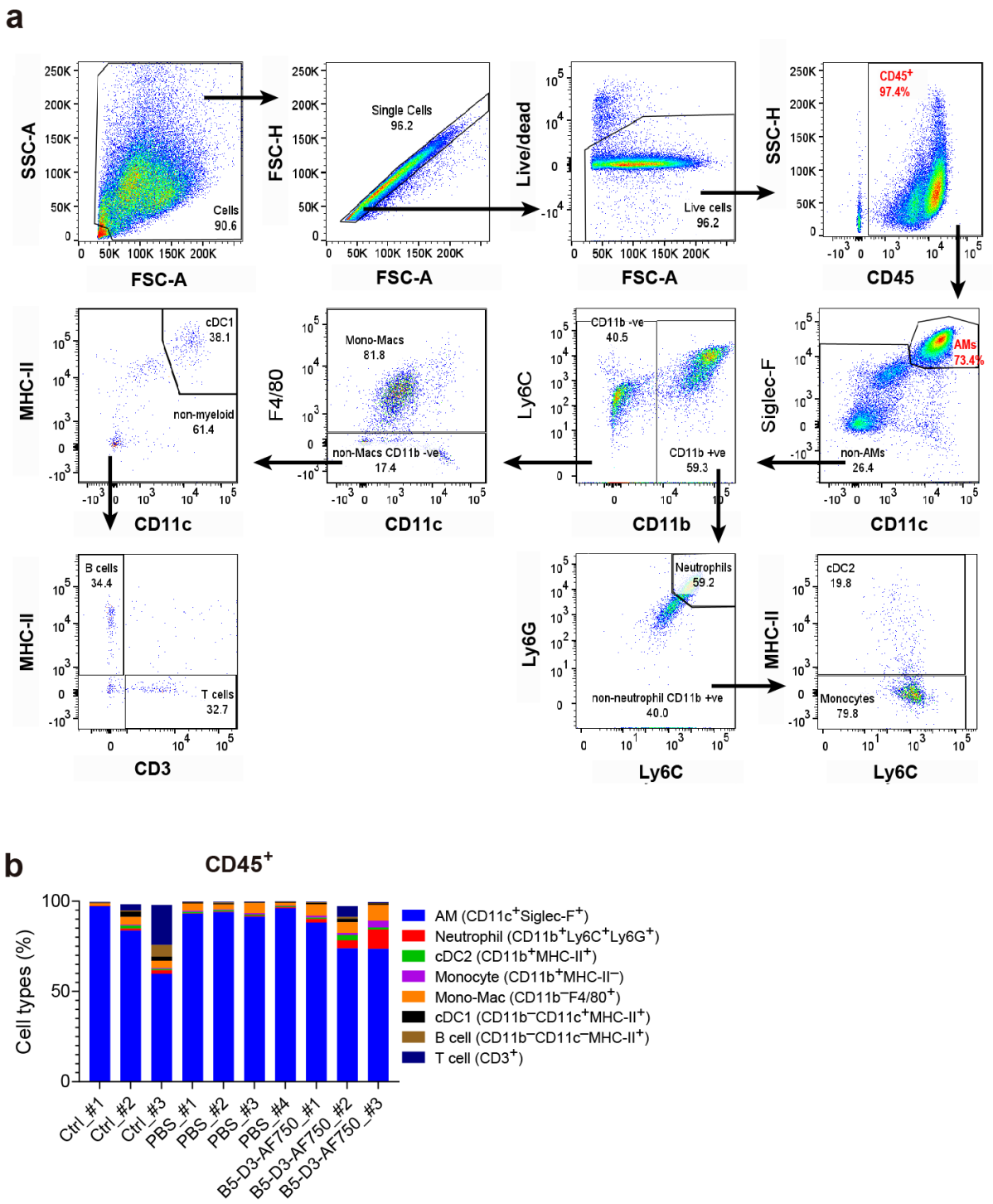

Supplementary Fig. 12 Flow cytometry analysis of mouse BALF cells. a Flow cytometric gating strategy for BALF cells. **b** Percentages of individual cell types in CD45^{+} BALF cells collected from individual animals. Ctrl group received no treatment before sacrifice.

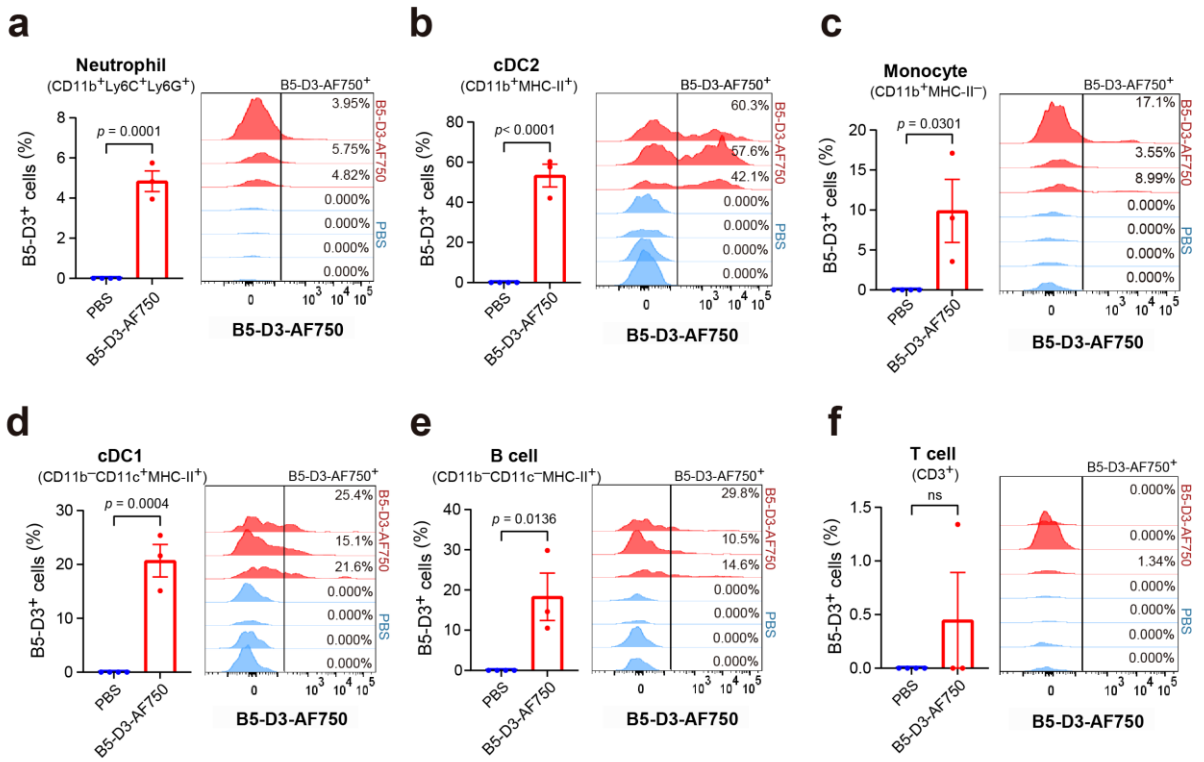

Supplementary Fig. 13 Binding/uptake rates of B5-D3-AF750 in BALF cells. a–f Positive rates (left) and histograms (right) of B5-D3 binding/uptake as indicated by B5-D3-AF750 fluorescence intensities in $CD11b^{+}Ly6C^{+}Ly6G^{+}$ neutrophils (**a**), $CD11b^{+}MHC\text{-}II^{+}$ cDC2 (**b**), $CD11b^{+}MHC\text{-}II^{-}$ monocytes (**c**), $CD11b^{-}CD11c^{+}MHC\text{-}II^{+}$ cDC1 (**d**), $CD11b^{-}CD11c^{-}MHC\text{-}II^{+}$ B cells (**e**), and $CD3^{+}$ T cells (**f**). B5-$D3^{+}$ rates from individual mice are indicated on histograms. Data are presented as mean ± SEM, and statistical significance was determined by Student's t-test.

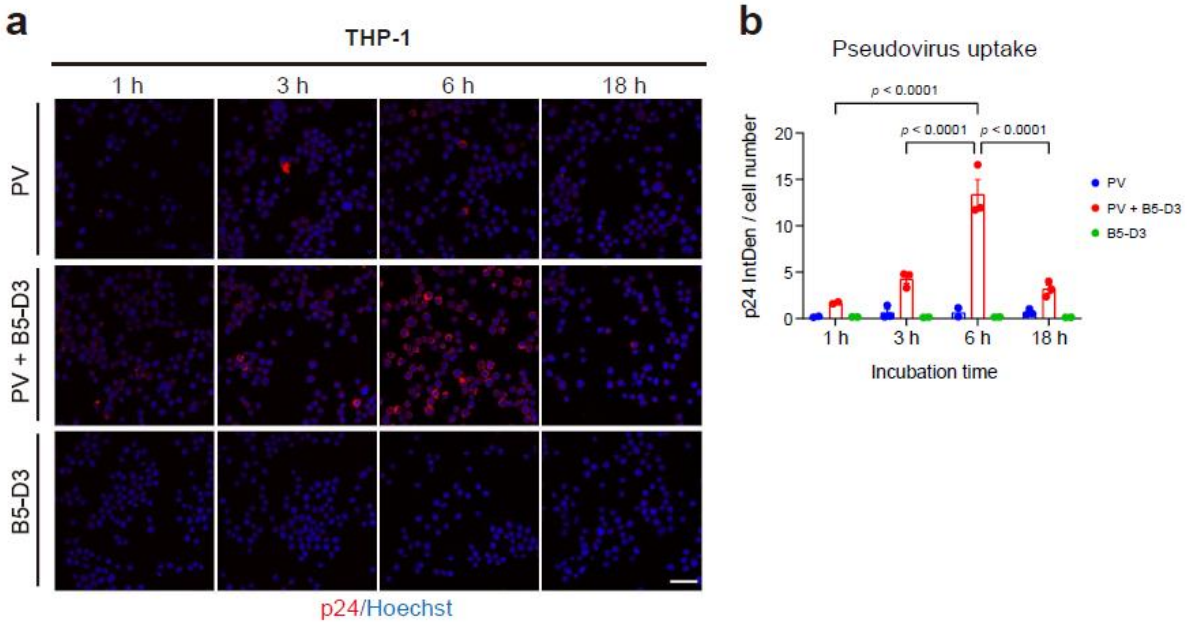

Supplementary Fig. 14 Time-course analysis of sACE2-Fc-dependent pseudovirus entry in THP-1 cells. a Representative image showing B5-D3-mediated phagocytosis of pseudovirus by THP-1 monocytes at various time points (1, 3, 6, and 18 h). Cells were incubated with pseudovirus and B5-D3, followed by immunostaining for p24 (red, Invitrogen # PA5-81773). **b** Quantification of mean p24 signal intensity per cell as shown in **a**. IntDen per cell number indicates the average p24 signal per cell, analyzed using ImageJ. Each dot represents one image.

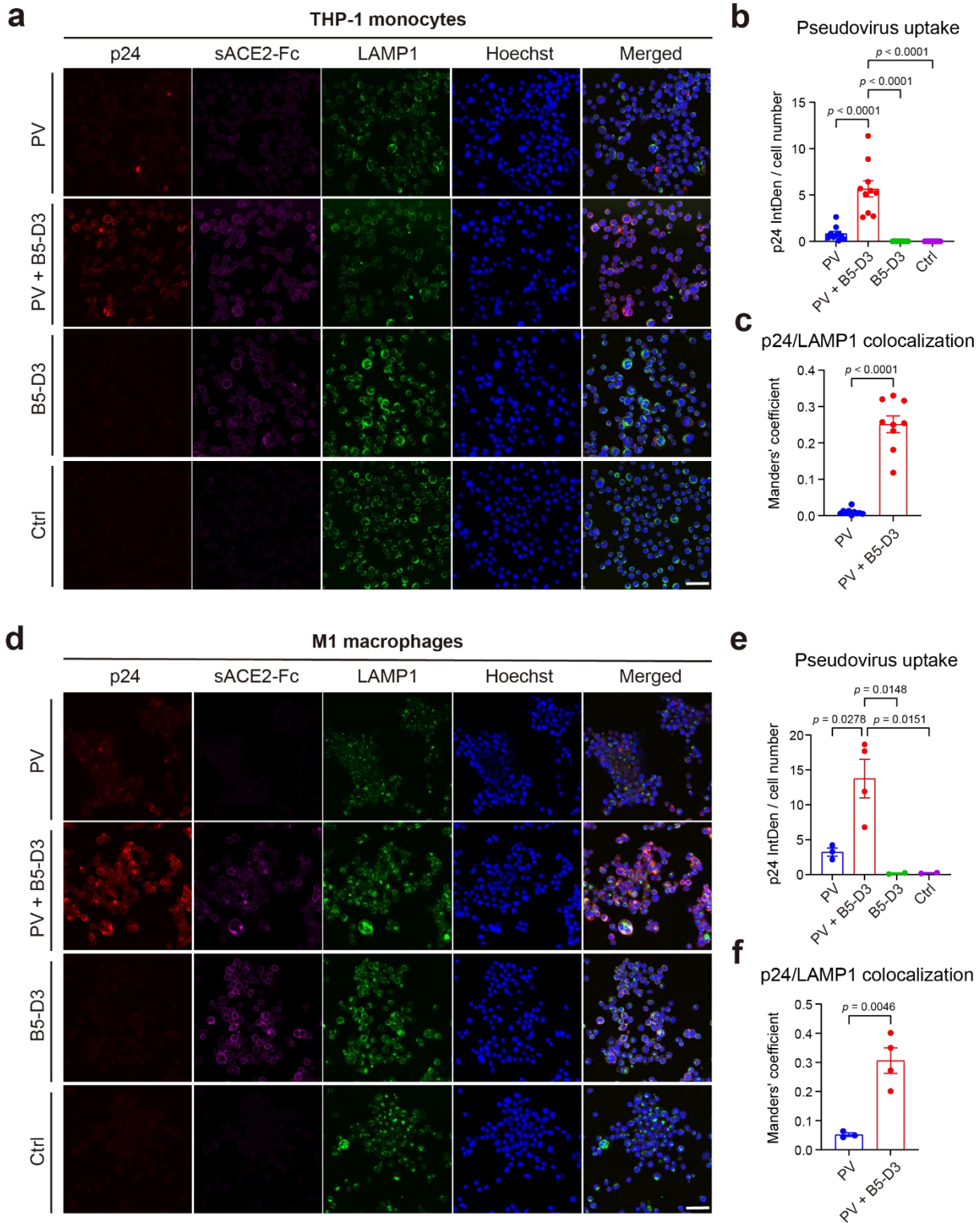

Supplementary Fig. 15 Enhanced phagocytosis of SARS-CoV-2 pseudovirus by THP-1 and THP-1-derived macrophages facilitated by sACE2-Fc. a, **d** Representative images illustrating phagocytosis of SARS-CoV-2 pseudovirus by THP-1 monocytes (**a**) and THP-1 differentiated M1 macrophages (**d**) after 6 hours of incubation with or without sACE2-Fc (scale bar = 50 µm). p24 (Invitrogen # PA5-81773) and LAMP1 (Abcam # ab25630) were used to identify the pseudovirus and lysosomes, respectively. **b**, **e** Quantification of mean p24 signal intensity per cell for THP-1 monocytes (**b**) and M1 macrophages (**e**). IntDen per cell number indicates the mean p24 signal per cell, analyzed using ImageJ. Each dot represents one image. **c**, **f** Manders'

coefficient demonstrating the colocalization of p24 and LAMP1 in THP-1 monocytes (**c**) and M1 macrophages (**f**). Data are presented as mean ± SEM, and statistical significance was determined by Tukey's multiple comparisons test.

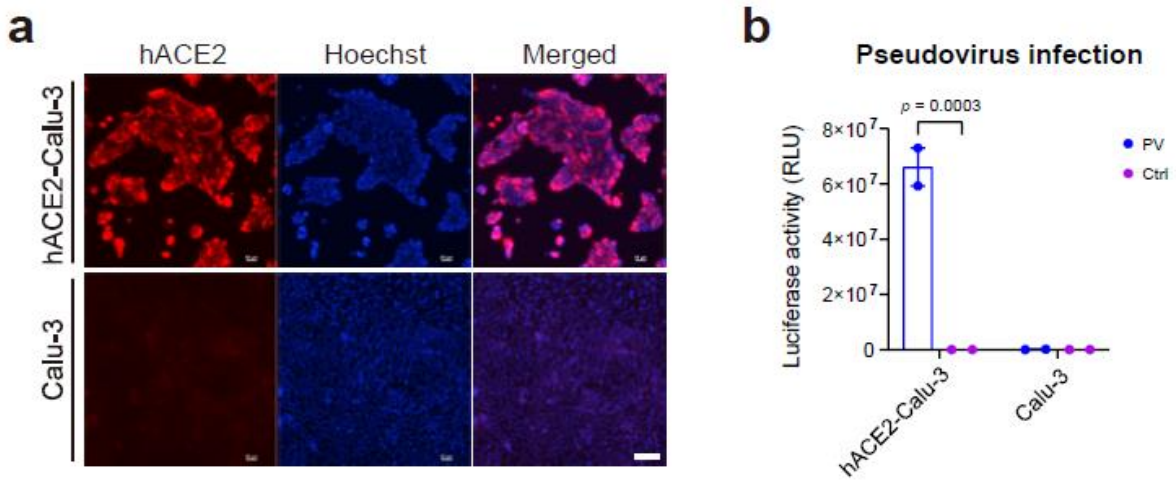

Supplementary Fig. 16 Generation of Calu-3 cell overexpressing hACE2 for enhanced pseudoviral infection. a Immunostaining of hACE2 (Abcam # ab15348) in hACE2-Calu-3 and control Calu-3 cells. **b** Infection levels of SARS-CoV-2 pseudovirus in hACE2-Calu-3 versus control Calu-3 cells, quantified by luciferase assay 72 hours post-infection, performed in duplicate. Data are presented as mean ± SEM, and statistical significance was determined by Šídák's multiple comparisons test.

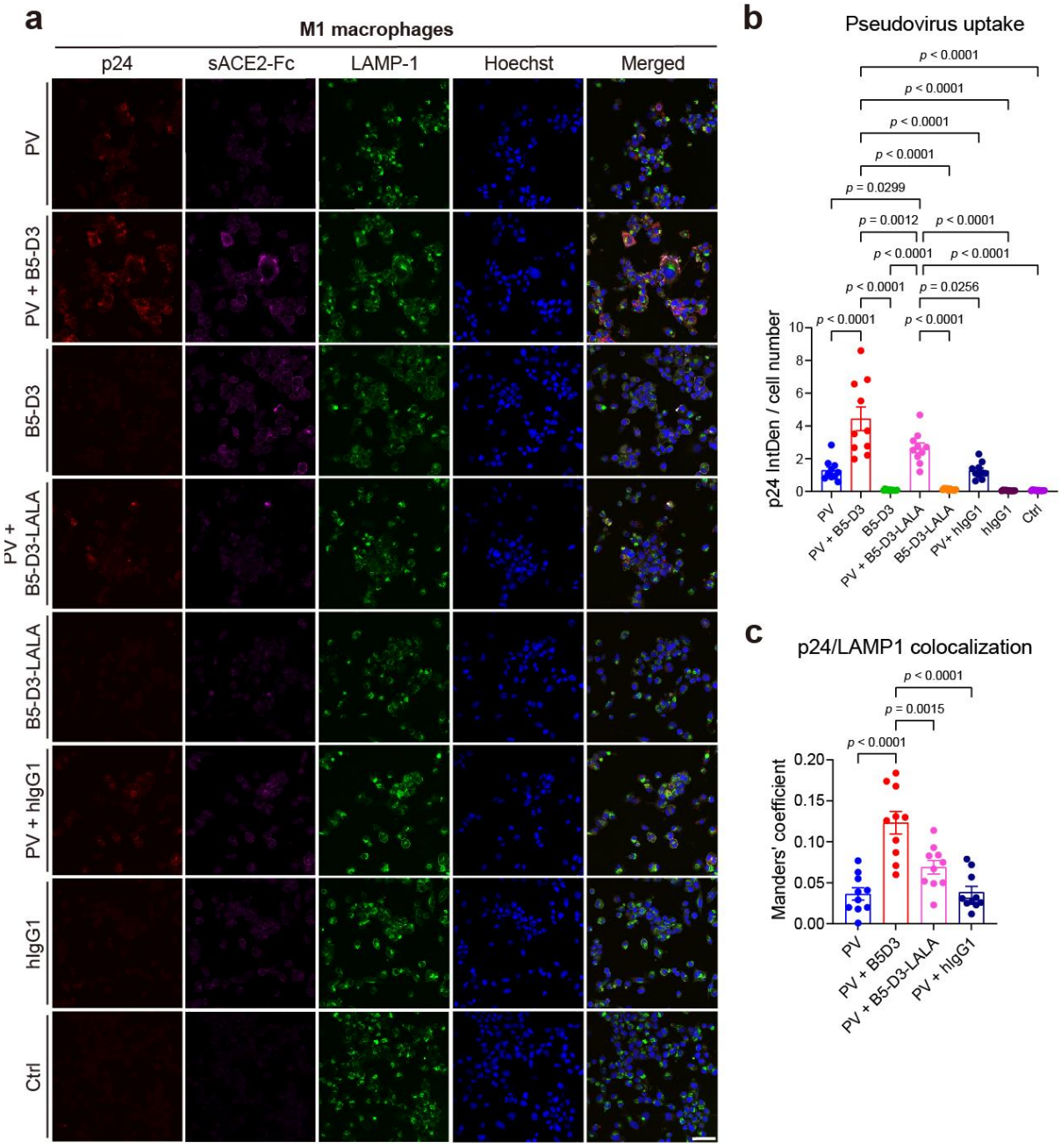

Supplementary Fig. 17 Reduced uptake of SARS-CoV-2 pseudovirus in THP-1-derived macrophages due to malfunction or absence of Fc domain in B5-D3. a Representative images illustrating uptake of SARS-CoV-2 pseudovirus (PV) by THP-1-derived M1 macrophages at 6 h after incubation with B5-D3, B5-D3-LALA, and hIgG1 isotype with or without PV. Scale bar = 50 µm. **b** Quantification of mean p24 signal intensity per cell. IntDen per cell number indicates the mean p24 signal per cell, analyzed using ImageJ. Each dot represents one image. Data are presented as mean ± SEM, and statistical significance was determined by Tukey's multiple comparisons test.

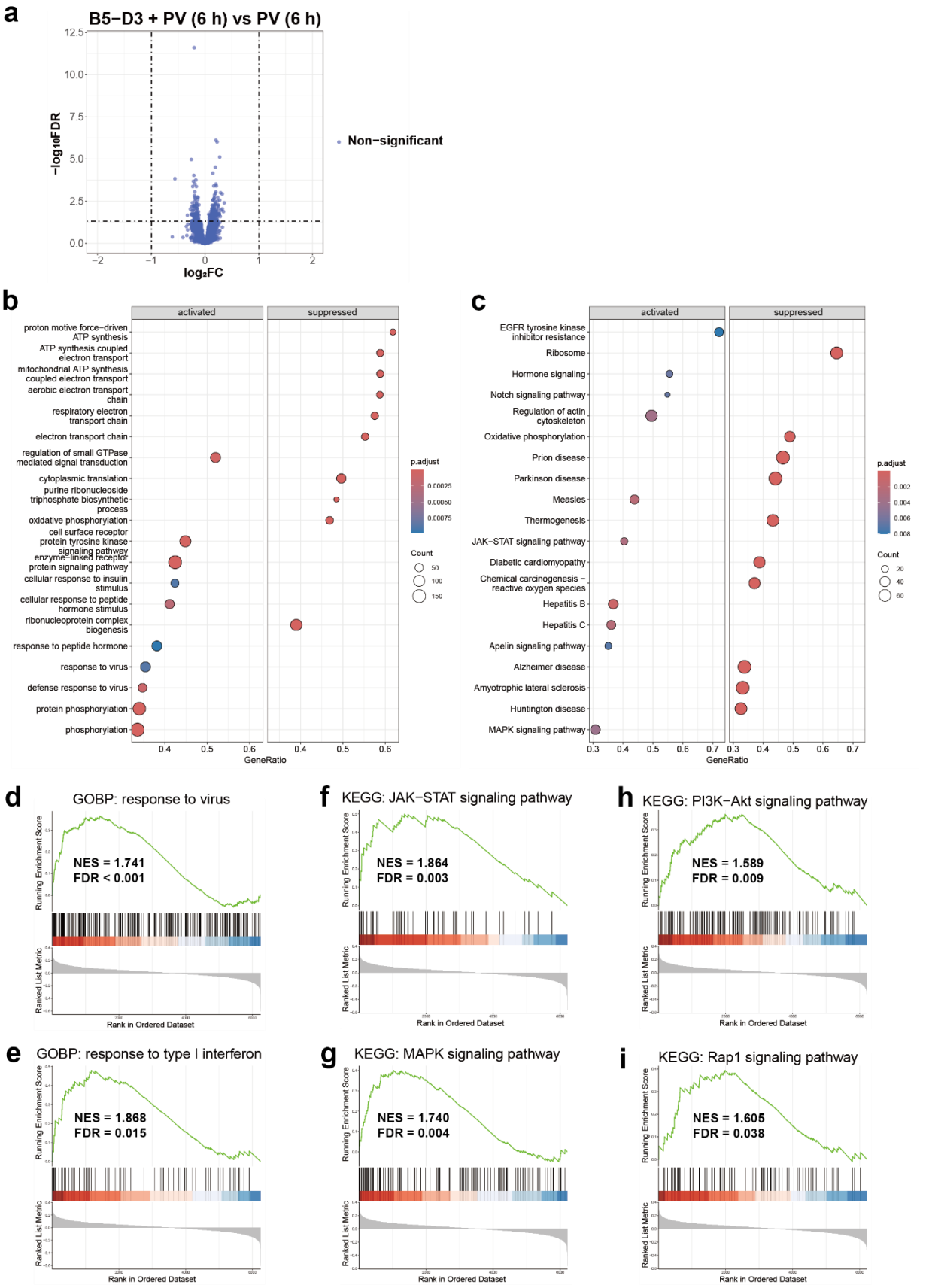

Supplementary Fig. 18 Transcriptomic analysis revealed activation of THP-1-derived macrophages mediated by 6 h incubation with B5-D3-pseudovirus complex. a DGE analysis between THP-1-derived M0 macrophages incubated with B5-D3 + pseudovirus (PV) and those

incubated with PV only (incubation time = 6 h). **b** GSEA of GOBPs significantly altered in the B5-D3 + PV group compared to the PV group, with top 15 most significantly activated and top 15 most significantly suppressed terms displayed. **c** GSEA of KEGG pathways significantly altered in the B5-D3 + PV group compared to the PV group, with top 15 most significantly activated and top 15 most significantly suppressed terms displayed. **d**–**i** GSEA plots of response to virus (**d**), response to type I interferon (**e**), JAK-STAT signaling pathway (**f**), MAPK signaling pathway (**g**), PI3K-Akt signaling pathway (**h**), and Rap1 signaling pathway (**i**) in B5-D3 + PV vs PV comparison. Benjamin–Hochberg method was used for FDR adjustment.

Supplementary Table 1. Enhanced tolerance and stability of B5-derivatives compared to WT sACE2-Fc in AAV-administered K18-hACE2 mice. Detailed *post hoc* comparisons among treatment groups shown in Supplementary Fig. 4b. Diff., difference; **, $0.001 \leq p < 0.01$; *, $0.01 \leq p < 0.05$. *p* values were determined by Tukey's multiple comparisons test.

Tukey's multiple comparisons test	Mean Diff. (ng/mL)	Adjusted *p*	Summary
PBS vs. WT	-9990	0.0017	**
PBS vs. B5-D3	-29104	0.0046	**
PBS vs. B5-D4	-29894	0.0028	**
PBS vs. B5-D5	-26774	0.0013	**
WT vs. B5-D3	-19114	0.0145	*
WT vs. B5-D4	-19904	0.0078	**
WT vs. B5-D5	-16784	0.0021	**
B5-D3 vs. B5-D4	-790.4	0.9459	ns
B5-D3 vs. B5-D5	2330	0.4915	ns
B5-D4 vs. B5-D5	3120	0.2103	ns

Supplementary Table 2. Primers used in quantitative PCR.

Primers	Sequences
SARS-CoV-2 *S*	CGTCAGGCTGTTTAATAGGGGC
	GACTAGCTACACTACGTGCCCGC
SARS-CoV-2 *N*	CAATGGCGGTGATGCTGCTCTTG
	TTCTGGACCACGTCTGCCGAAAG
AAV copies	AGCCGGAGAACAACTACAAG
	CCAACACACAGATCTAATG
Mouse *Gapdh*	GGGCATCTTGGGCTACACTGAGGACCAG
	CACCCTGTTGCTGTAGCCGTATTCATTGTC